High-Fidelity Reduced-Order Aerodynamic Models: Application to Active Control of Engine Inlets

by

Guillaume LASSAUX
Ingénieur diplômé de l'Ecole Polytechnique (2000)

Submitted to the Department of Astronautics and Aeronautics
in partial fulfillment of the requirements for the degree of

Master of Science in Astronautics and Aeronautics

at the

MASSACHUSETTS INSTITUTE OF TECHNOLOGY

June 2002

Author .....
Department of Astronautics and Aeronautics
May 24, 2002

Certified by .....
Karen E. Willcox
Assistant Professor
Thesis Supervisor

Accepted by .....
Wallace E. Vander Velde
Professor of Aeronautics and Astronautics
Chair, Committee on Graduate Students

High-Fidelity Reduced-Order Aerodynamic Models: Application to Active Control of Engine Inlets

by

Guillaume LASSAUX

Ingénieur diplômé de l'Ecole Polytechnique (2000)

Submitted to the Department of Astronautics and Aeronautics
on May 24, 2002, in partial fulfillment of the
requirements for the degree of
Master of Science in Astronautics and Aeronautics

Abstract

An unsteady Euler flow solver is developed for subsonic and supersonic duct flows. A linearized solver is derived from the nonlinear set of equations. Results show the accuracy of both formulations. Arnoldi-based model order reduction is reviewed. Both single and multiple frequency point Arnoldi methods are presented. An orthogonal reduced-order basis is generated by iterating system matrices on the input vector at a set of selected points. The full-order system is then projected onto the reduced space. The resulting reduced-order model obtained matches moments of the original model transfer function at each frequency point selected. A specific implementation procedure is presented for a system with singular descriptor matrix, which arises from boundary conditions. A state space system is extracted from the algebraic system and boundary conditions are accounted for in the output via a feedthrough term.

Results are presented for linearized analysis of a started supersonic diffuser. Both single point and multiple point Arnoldi methods are applied. The size of the reduced-order models is decreased by two orders of magnitude over the computational fluid dynamics model, while preserving accuracy of the relevant dynamics. Moreover, multiple point Arnoldi outperforms the single point method, and allows a further reduction in the number of states while offering a balance between model size and computational cost. The reduced-order models are used for active shock position control via bleed. The derived controller is shown to be effective for the full-order model, and the dynamics of interest are accurately captured.

Thesis Supervisor: Karen E. Willcox
Title: Assistant Professor

Acknowledgments

Here comes the time when I can free myself from all the conventions of scientific writing. A few lines to thank all the ones that brought support, help and life to these two years.

My advisor, Karen, has made the present thesis what it is. Whatever the time, whatever the question (sometimes silly. After all, I am only 24!), she always took the time to listen and pull me out of the glue I was stuck in. As I learned, research is a hidden track and misleading highways are so tempting. Like the dedicated Ranger, she guided my steps to this thesis. Thanks to Professor Jaime Peraire, who took care of me for one whole year before I was able to bring CFD plots that made sense. I am also very grateful to Professor Mark Drela, for his insights into computational fluid dynamics. Many problems, many questions and many answers. I still keep thinking that one single student brain is not enough to manage one whole CFD code. I would like to mention Professor Alexandre Megretski, who had a strong input into my work and give me many insights into control design and model-order reduction.

Thanks to Jim Paduano and all the members of the Quiet Supersonic Project team who showed interest for my work. They offered a wonderful application to my CFD code I struggled with for so long. This project gave my research work the diversity I hoped for.

All the ACDL crew have made my stay in this lab the unforgettable experience it was. Thanks to Victor, Tolu and Angie for their time and patience whenever Unix system did not recognize me as one of his disciples. I would like to mention Jean, whose dedication and efficiency makes a difference every day.

Thanks to Joe, my favorite Canadian, who adopted me like an abandoned dog two years ago and taught me everything a first year graduate student should know about managing practical life at MIT. Joe, I am leaving before you do, but hang on,

you're almost done!

Many friends were present during these two years. Thanks to them all. Actually, I did not feel all that lonely even though I was far from home! I am also very grateful to Anne-Christelle for the time we spent sharing our stories, our questions and our answers (which unfortunately were not as numerous as the questions).

I cannot think about Boston without thinking about my three roommates, David, Vincent and Xavier. So many moments shared, in Boston as well as in San Francisco and Montreal. I hope that many more moments and places will follow.

My last words will be for my parents, Stéphane and Jean, my brother, Pierre, and my sister, Blandine. I am grateful to them for encouraging me in this American experience whenever I needed motivation. Although I was one ocean away, I still felt close to each one of you.

Contents

List of Figures

Chapter 1

Introduction

Computational fluid dynamics (CFD) has reached a considerable level of maturity and is now routinely used in many applications for both external and internal flows. Methods based on the discretization of the Euler and Navier-Stokes equations enjoy widespread use for aerodynamic design and analysis, and provide accurate answers for a variety of complex flows. However, ensuring model accuracy requires that the flow domain is finely discretized, especially in regions where the flow characteristics undergo rapid variations. Despite ever increasing computational power, nonlinear unsteady problems are computationally very expensive and time-consuming. At each time step, several matrix inversions need be performed to solve the set of nonlinear equations via Newton's method. More efficient methods for time-varying flow can be obtained if the disturbances are small, and the unsteady solution can be considered to be a small perturbation about a steady-state flow [12]. In this case, a set of linearized equations is obtained which can be time-marched to obtain the flow solution at each instant. Since most of the computing cost involved by nonlinear flow solvers lies in matrix inversions, a substantial gain is obtained from linearized method as the system Jacobian only needs to be evaluated and inverted once.

Even under the the linearization assumptions, any CFD-based technique will generate models with a prohibitively high number of states. For this reason, CFD models are not appropriate for many applications where model size and cost are issues. Coupling the aerodynamic solver with another disciplinary model is sometimes not

practicable. For example, in aeroelastic analysis [25], a common approach is to simultaneously march the fluid dynamics and the structural dynamics equations. Such a method couples two high-order dynamical systems and becomes computationally very expensive. Low-order models that approximate the full-order dynamical system with good accuracy are of great interest. Another application which requires low-order models is control design.

The concept of using active control to enhance the stability properties of an unsteady flow has been addressed for several applications, such as stabilization of compressor surge in jet engines [7, 19]. In order to derive control models that will be effective, it is vital that the relevant unsteady flow dynamics are captured accurately. A model is required that will capture not only the dynamics of the disturbance to be controlled, but also the visibility offered by the sensing and the effect on the flow of the actuation mechanism. A high-fidelity CFD code can offer the degree of flow resolution required. However, applying modern control theory becomes a real challenge. Optimal control design involves solving the Riccati equations of dimension n, where n is the dimension of the dynamical system. The cost of computing these solutions is order n^3. Therefore, it is imperative that the flow model have a low number of states.

One approach to creating more efficient flow models is to make a set of physically-based simplifying assumptions about the flow. The flow is typically assumed to be two-dimensional and potential. In the context of aeroelastic simulations, efficient semi-analytic models for lightly loaded thin blades have been developed for subsonic flow [26], and for supersonic flow [1]. These models prove to be useful near design conditions. However, they yield reduced fidelity results for off-design conditions, as blade loading effects become important [25]. Moreover the validity of such models does not extend to all flow regimes. In particular, the modeling of transonic flows poses a difficulty.

Model reduction is one approach to obtaining efficient, low-order models while retaining the high-fidelity flow dynamics of CFD. The basic idea is to project the high-fidelity CFD solutions onto a set of basis functions which span the flow solution space efficiently. Models are obtained which retain the high-fidelity aerodynamics

of the CFD analysis, but which have only a few states. One possibility for a basis is to compute the eigenmodes of the system [13]. However, typical problem sizes are on the order of tens of thousands of degrees of freedom even in two dimensions, and solution of such a large eigen-problem is in itself a very difficult task. The proper orthogonal decomposition technique (POD) has been developed as an alternate method of deriving the basis functions [24, 4]. Based on selected snapshots of the flow, the POD-generated reduced basis aims at describing the flow solution with high accuracy over the frequency range of interest. These snapshots can be obtained from time domain simulations [22] or, less expensively, derived in the frequency domain by exploiting the linearity of the governing equations [15]. Frequency domain POD-based reduced order model have been developed to compute the aeroelastic behavior of transonic airfoils and turbomachinery [11, 28]. Active control models have also been derived using POD for vortex shedding [8, 9]. Reduced-order modeling applications for linear flow problems using eigenmodes and POD are reviewed by Dowell et al. [5].

Krylov subspace based methods are an alternative to the POD method for generating a reduced-order basis. The Arnoldi algorithm can be used to generate a set of vectors which forms an orthonormal basis for the Krylov subspace. The resulting reduced-order models match moments of the CFD system transfer function. One can liken the moment-matching techniques to matching the transfer function and its derivatives at a particular frequency (usually zero). If q basis vectors are included in the reduced-order model, then q moments of the transfer function will be matched. Arnoldi-based reduced-order models have been developed for RLC circuits [23] and compressor aeroelastic models [27]. Arnoldi-based reduced-order models have been used also in active control design, for the sensor/actuator placement problem [2]. Because the vectors are derived at a single frequency point, the Arnoldi approach is computationally much cheaper than the POD. Multiple frequency point Arnoldi methods have also been developed [10] and applied to circuit simulations [20]. The idea here is to select multiple frequency points about which to match moments. Once again, multiple vectors are evaluated at each frequency point, and the number of moments matched at each point is equal to the number of vectors included in the

basis. The computational expense of deriving the model increases with the number of frequency points used, however using several interpolation points typically reduces the size of the resulting reduced-order model. The multiple-point Arnoldi method therefore provides a way to trade computational expense of model derivation and size of reduced-order model.

All of the model order reduction techniques described so far are limited to linear time invariant (LTI) systems. Nonlinear effects are neglected, which restricts the range of validity of the reduced models to small perturbations about steady state. Some approaches have been investigated to model nonlinear effects but most of them still require evaluation of the full-order nonlinear residual, which makes them computationally expensive. For example in [16], POD is used to derive a nonlinear reduced-order model for aeroelastic analysis of a panel in a transonic flow. However, piecewise-linear reduced order models have been recently developed [21]. A 'training' input is given as input to the nonlinear system and Arnoldi reduced-order models are constructed at successive points of the nonlinear trajectory. This method has been applied successfully to highly nonlinear systems, such as micromachined beams and nonlinear electrical circuits [21].

In this work, linear Arnoldi-based reduced-order models will be generated to simulate flow variations in an actively-controlled started supersonic diffuser. Such diffusers are designed to decelerate the incoming supersonic flow to subsonic speed. This mechanism enables compression of the air before it enters the compressor of a jet engine. Depending on the design, a normal shock may form right behind the throat: in this case, the supersonic diffuser is started. A started supersonic diffuser is sketched in Figure 1-1.

The incoming flow is subject to perturbations due to atmospheric disturbances, which can cause expulsion of the normal shock towards the inlet. This mechanism is also known as unstart. An unstart results in a loss of propulsive efficiency and a dramatic increase in the drag undergone by the airplane. One-dimensional linear analysis procedures have been developed and used to analyze inlet unstart [17] and have shown that the tolerance to unstart can be increased by increasing the rate of

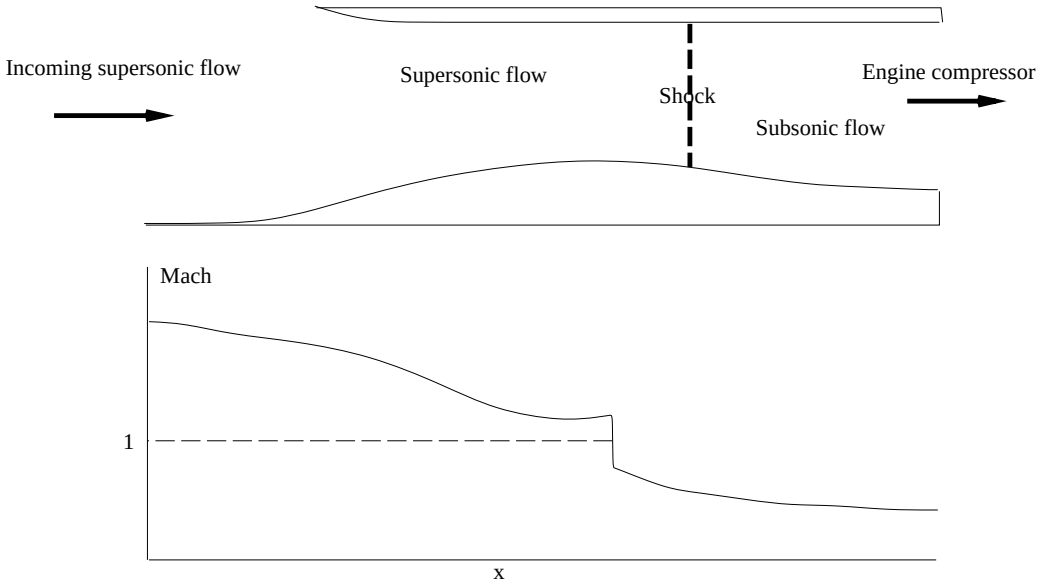

Figure 1-1: Top: Started flow in supersonic diffuser. A shock forms behind the throat. Bottom: Sketch of average Mach number against streamwise coordinate, x.

throat bleed (mass flow dumping between the throat and the normal shock). However, to correctly model the influence of mass flow dumping, 2-D effects need be accounted for, as bleed is a relevant actuation mechanism for unstart control.

In order to derive an effective control model, reduced-order models are needed that capture the dynamics associated to the atmospheric disturbances and the effect of bleed. The two-dimensional linearized Euler equations will be considered here, however the approach could be extended to three-dimensional and viscous models if the underlying CFD model were available. This study could also extend to nonlinear using the piecewise-linear approach. Frequency domain calculations will be used to derive the reduced-order basis efficiently. However, the reduced-order model will be developed in the time domain and cast in state-space form, which allows for ease of coupling to the active control model.

Chapter 2 will present an Euler unsteady flow solver. This CFD model will be used to simulate subsonic and supersonic duct flows with second order accuracy. Validation results will show the high-fidelity of the model. A linearized CFD model will then be derived from this nonlinear flow solver. Validation results will be performed that show

agreement between the nonlinear and the linear flow solver for small perturbations. Examples will be presented which demonstrate the limits of the linearized solver as nonlinear effects become important in the flow.

Chapter 3 will review the basics of Arnoldi-based model order reduction techniques. We will present both single point and multiple point Arnoldi methods. Two algorithms will be derived to make implementation of the methods systematic. In order to enable application of these algorithms to the CFD model, we will generalize the methods to singular descriptor matrix systems.

Chapter 4 will present applications of Arnoldi-based order reduction techniques to a supersonic diffuser. Single and multiple point Arnoldi methods will be applied and two post-processing procedures will be investigated in order to generate the reduced basis. The resulting reduced-order models will be used to design a simple controller. Results will be presented which demonstrate the effectiveness of the controller on the full-order system.

Finally, in Chapter 5, we will present conclusions and directions of future work.

Chapter 2

Computational Model

This chapter will describe an unsteady formulation to simulate subsonic and supersonic flows in an engine inlet. This inlet is designed to provide a compressor with air at the required conditions. Although the formulation to be explained has subsonic capability, most of the work will focus on supersonic inlet flows. Ultimately, this computational tool will be used for active shock control design, in order to prevent inlet unstart. Figure 2-1 shows the physical representation of the problem. A supersonic inlet flow is decelerated from the inlet plane to the throat, behind which a shock forms. Downstream of the shock, the flow is subsonic.

We will describe an inviscid two-dimensional unsteady formulation based on a finite volume method developed on the computational domain showed showed in Figure 2-1. This code is an enhancement of MSES, a steady potential flow solver designed by Mark Drela [6]. This steady solver generates a structured grid, whose streamwise gridlines are unknowns of the numerical scheme and are constrained so that they approximate the flow streamlines. This steady solver therefore specifies the flow velocity with knowledge of the gridline direction and the streamtube mass flow, which is constant in steady flows. Streamwise gridlines and streamtubes can be seen in Figure 2-1.

We make use of MSES to grid our computational domain and initialize the flow quantities. However, the grid computed with the steady solver is frozen for unsteady computations and is no longer an unknown. In the unsteady formulation, the flow

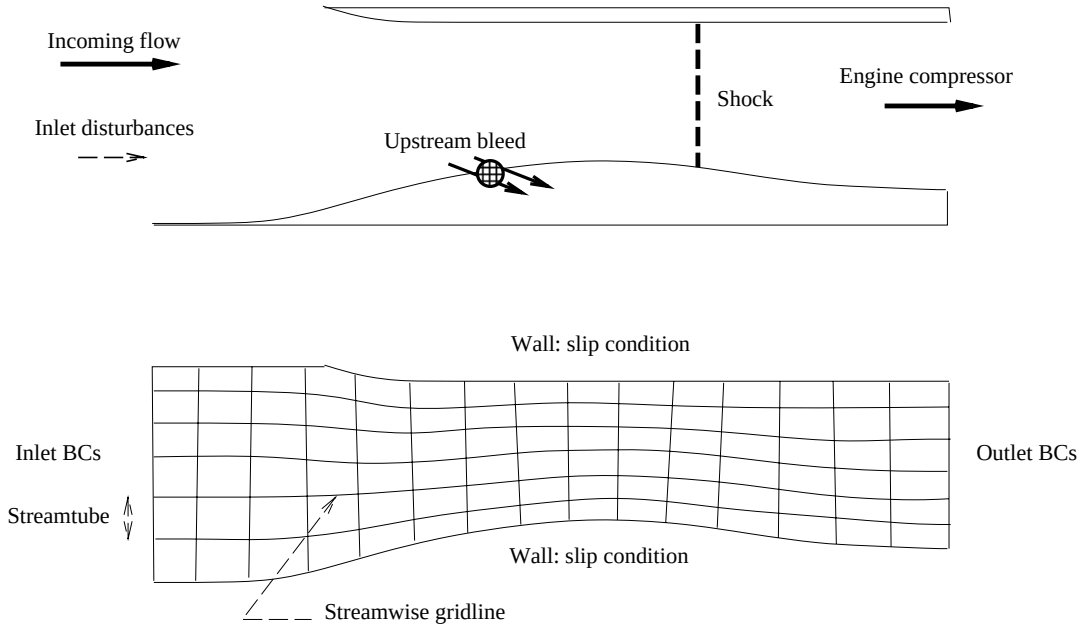

Figure 2-1: Presentation of physical system. Top: supersonic flow with shock at the throat (started inlet). Bottom: computational domain for finite-volume formulation.

velocity is specified via its projections on both the streamwise gridline and the normal-to-gridline direction, as seen on Figure 2-2.

2.1 Discretization of Unsteady Euler Equations

2.1.1 Unsteady Euler Equations

The discrete Euler equations are derived from the integral form of the unsteady, two-dimensional equations, which are the usual statements of mass, momentum, and energy:

$$\frac{\partial}{\partial t}\iint \rho \, dV \;+\; \oint dm \;=\; 0 \tag{2.1}$$

$$\frac{\partial}{\partial t}\iint \rho\vec{Q} \, dV \;+\; \oint \vec{Q} \, dm \;+\; \oint p \, d\vec{A} \;=\; 0 \tag{2.2}$$

$$\frac{\partial}{\partial t}\iint \rho E \, dV \;+\; \oint H \, dm \;=\; 0 \tag{2.3}$$

where the flow variables are defined as follows:

ρ density

$\vec{Q}$ total velocity vector

p pressure

H total enthalpy

E energy

and $dm = \rho \vec{Q} \cdot d\vec{A}$ is the mass flux element across the moving conservation cell boundary . $d\vec{A} = dA\hat{n}$ where dA is a surface element and $\hat{n}$ a unit vector pointing outward the control volume.

The discrete Euler equations approximate the integral form of the continuous Euler equations on small control volumes or control cells. The flow velocity is fully specified with the knowledge of the q's and $q_\perp$'s, which are the projections of $\vec{Q}$ on the streamwise gridline and the normal-to-gridline directions respectively as seen on Figure 2-2. The state variables are chosen to be

q streamwise component

$q_\perp$ normal component

ρ density

H total enthalpy

and are located at the grid positions shown in Figure 2-2. In contrast with other state variables, $q_\perp$ is not located at the midpoints of the cell faces but at their vertices. This location actually simplifies the imposition of the no-slip conditions at the wall as we will see later on in this section.

The geometric grid nodes x, y define the conservation-cell face vectors $\vec{a}$, $\vec{b}$, which connect the midpoints of the grid segments. Both vectors are the boundaries of the control cell, whose meanline direction is meant to approximate the steady streamline. The finite volume formulation to be used requires that the flow quantities at the midpoints of each of these vectors are known. To fully specify the velocity direction at the midpoint of $\vec{a}$ we define the vector $\vec{s}$, which connects the midpoints of the

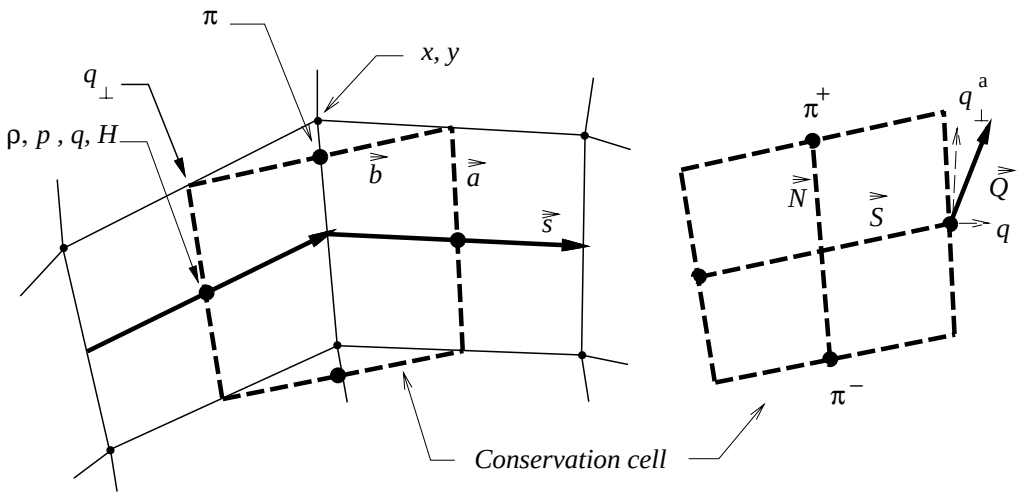

Figure 2-2: Geometric grid (solid lines), conservation cell (bold dashed lines), and variable locations.

quasi-normal gridline segments. $\vec{s}$ is supplemented with $\vec{s}_\perp$, so that $(\vec{s},\, \vec{s}_\perp)$ be an orthogonal basis. Similarly we define $\vec{b}_\perp$ at the midpoint of $\vec{b}$, so that $\left(\vec{b}\,,\, \vec{b}_\perp\right)$ be an orthogonal basis as well. Other useful geometric quantities are defined as follows:

$$\hat{s} = \frac{\vec{s}}{|\vec{s}\,|} \qquad \text{streamwise unit vector}$$

$$\hat{b}^+ = \frac{\vec{b}^+}{|\vec{b}^+|} \qquad \text{upper streamwise unit vector}$$

$$\hat{b}^- = \frac{\vec{b}^-}{|\vec{b}^-|} \qquad \text{lower normal unit vector}$$

$$\vec{S} = \tfrac{1}{2}\left(\vec{s}_i + \vec{s}_{i-1}\right) \qquad \text{mean streamwise vector}$$

$$\vec{N} = \tfrac{1}{2}\left(\vec{a}_i + \vec{a}_{i-1}\right) \qquad \text{mean quasi-normal vector}$$

$$A = |\hat{s} \times \vec{a}| \qquad \text{area seen by streamwise component}$$

$$A_\perp = |\hat{s_\perp} \times \vec{a}| \qquad \text{area seen by normal component}$$

$$V = |\vec{S} \times \vec{N}| \qquad \text{conservation-cell volume}$$

All state variables are located at the midpoints of the $\vec{a}$, $\vec{b}$ cell-face vectors, except the $q_\perp$'s, which are located at the vertices of the conservation cell. These are averaged at the midpoints of the $\vec{a}$, $\vec{b}$ to calculate the flow quantities $\vec{Q}$, H, etc. When defining these flow quantities, it is important to distinguish between the quantities defined at the midpoints of the $\vec{a}$ and those defined at the midpoints of the $\vec{b}$. Based on the integral Euler equations (2.1-2.3), the finite volume formulation requires that we know

the fluxes of mass, momentum and energy through the cell faces. At the midpoint of $\vec{a}$, the flow quantities are as follows:

$$\vec{q}^{\,a} \;=\; q^a\,\hat{s} \qquad \text{streamwise component of velocity}$$

$$q^a_\perp \;=\; \tfrac{1}{2}\left(q^+_\perp + q^-_\perp\right) \qquad \text{streamwise component of velocity}$$

$$\vec{q}^{\,a}_\perp \;=\; q^a_\perp\,\hat{s_\perp} \qquad \text{normal component of velocity}$$

$$m^a \;=\; \rho^a\,(q^a A \;+\; q^a_\perp A_\perp) \qquad \text{streamwise mass flux}$$

$$\vec{Q}^{\,a} \;=\; \vec{q}^{\,a} \;+\; \vec{q}^{\,a}_\perp \qquad \text{absolute velocity}$$

$$p^a \;=\; \tfrac{\gamma-1}{\gamma}\,\rho^a\left(H^a \;-\; \tfrac{1}{2}(Q^a)^2\right) \qquad \text{pressure}$$

$$E^a \;=\; H^a \;-\; \tfrac{p^a}{\rho^a} \qquad \text{total energy}$$

where ρ^a, q^a and H^a are actually ρ, q and H as defined at the midpoint of $\vec{a}$. At the midpoint of $\vec{b}$, we average the downstream and upstream $q_\perp$. Moreover, q^b, H^b and entropy S^b are interpolated from the four surrounding $\vec{a}$ midpoints, using bilinear interpolation. The interpolation stencil is sketched on Figure 2-4. We also impose $\vec{q}^{\,b}$ to have the direction of $\vec{b}$.

$$\vec{q}^{\,b} \;=\; q^b\,\hat{b} \qquad \text{streamwise component of velocity}$$

$$q^b_\perp \;=\; \tfrac{1}{2}\left(q_{\perp i-1} + q_{\perp i}\right) \qquad \text{streamwise component of velocity}$$

$$\vec{q}^{\,b}_\perp \;=\; q^b_\perp\,\hat{b_\perp} \qquad \text{normal component of velocity}$$

$$\vec{Q}^{\,b} \;=\; \vec{q}^{\,b} \;+\; \vec{q}^{\,b}_\perp \qquad \text{absolute velocity}$$

Density and mass flux across $\vec{b}$ are computed through the following sequence:

$$h^b \;=\; H^b - \tfrac{1}{2}\left(Q^b\right)^2 \qquad \text{enthalpy}$$

$$\rho^b \;=\; e^{-S^b}\,\left(\tfrac{\gamma-1}{\gamma}h^b\right)^{\frac{1}{\gamma-1}} \qquad \text{density}$$

$$m^b \;=\; \rho^b\,b\,q^b_\perp \qquad \text{normal mass flux}$$

Figure 2-3 shows the vector relationships between $\vec{Q}$ and the q's and $q_\perp$'s.

Since $\vec{q}^{\,b}$ is parallel to $\hat{b}$, only $\vec{q}_\perp$ is accounted for when calculating the mass flux through $\vec{b}$. From now on we denote the x^a quantities by x_{i-1} if it is located at the midpoint of the upstream $\vec{a}_{i-1}$ vector, or x_i if located downstream. Similarly, x^b is

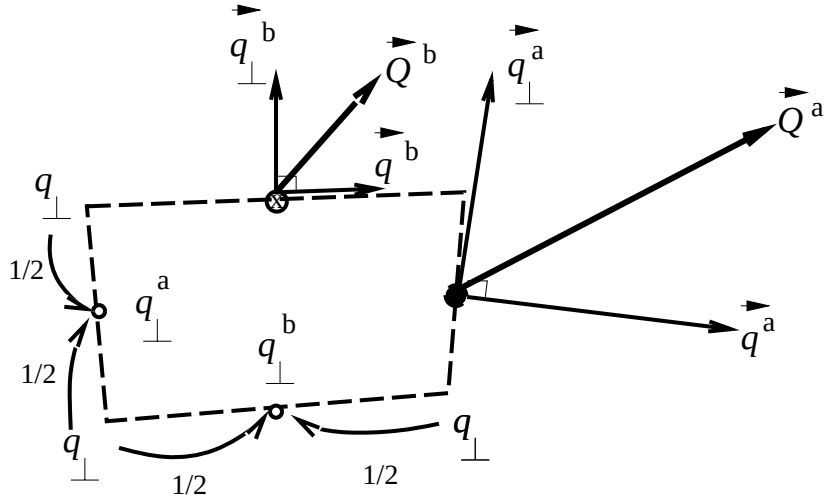

Figure 2-3: Decomposition of the flow velocity $\vec{Q}$ in the grid coordinate system, at the midpoints of the cell faces.

now denoted x^+ or x^-, if located on the top side or bottom side respectively.

An auxiliary pressure π is also defined at the midpoints of the $\vec{b}$ faces to distinguish it from the usual pressure p on the quasi-normal faces $\vec{a}$.

In the discrete system, it is convenient to define cell-average and cell-difference quantities, either between i and $i-1$, where $i-1$ and i refer to the left and right cell faces respectively. Such averaging are also defined for "+" and "−" variables, depending on the quantity involved.

$$p_a = \tfrac{1}{2}\left(p_i + p_{i-1}\right) \tag{2.4}$$

$$\pi_a = \tfrac{1}{2}\left(\pi^+ + \pi^-\right) \tag{2.5}$$

$$\Delta p = p_i - p_{i-1} \tag{2.6}$$

$$\Delta\pi = \pi^+ - \pi^- \tag{2.7}$$

$$\Delta^i m = m_i - m_{i-1} \tag{2.8}$$

$$\Delta^+ m = m^+ - m^- \tag{2.9}$$

The discrete form of the mass equation is then simply

$$\frac{\partial}{\partial t}\left(\rho_a V\right) + \Delta_i m + \Delta^+ m = 0 \tag{2.10}$$

The pressure integral on the conservation cell is discretized as

$$\oint p\, d\vec{A} \;=\; \left(p_i \vec{a}_i \;-\; p_{i-1}\vec{a}_{i-1} \;-\; \pi^+ \vec{b}^+ \;+\; \pi^- \vec{b}^-\right) \times \hat{k} \tag{2.11}$$

where $\hat{k}$ is the out-of-plane unit normal. Substituting

$$p_i \;=\; p_a \;+\; \tfrac{1}{2}\Delta p \qquad\qquad p_{i-1} \;=\; p_a \;-\; \tfrac{1}{2}\Delta p$$

$$\pi^+ \;=\; \pi_a \;+\; \tfrac{1}{2}\Delta \pi \qquad\qquad \pi^- \;=\; \pi_a \;-\; \tfrac{1}{2}\Delta \pi$$

gives the following

$$\oint p\, d\vec{A} \;=\; \left[p_a\, \Delta\vec{a} \;+\; \Delta p\, \vec{a}_a \;-\; \pi_a\, \Delta\vec{b} \;-\; \Delta\pi\, \vec{b}_a\right] \times \hat{k} \tag{2.12}$$

For consistency it is necessary to require that p and π approach the same value in the limit as the cell size shrinks to zero. A suitable requirement is

$$\pi_a \;=\; p_a \;+\; P_c \tag{2.13}$$

where P_c is a small higher-order "pressure correction" term which can be defined to suppress any possible odd-even $q_\perp$ modes.

The various geometry and grid-velocity quantities are related by the following identities and earlier definitions.

$$\Delta\vec{a} \;=\; \Delta\vec{b} \qquad\qquad \vec{N} \;=\; \vec{a}_a \qquad\qquad \vec{S} \;=\; \vec{b}_a \tag{2.14}$$

The pressure integral can now be written as

$$\oint p\, d\vec{A} \;=\; \left[-P_c\, \Delta\vec{a} \;+\; \Delta p\, \vec{N} \;-\; \Delta\pi\, \vec{S}\right] \times \hat{k} \tag{2.15}$$

and the semi-discrete form of the momentum equation is as follows

$$\begin{aligned} \frac{\partial}{\partial t}\left((\rho\vec{Q})_a\, V\right) \;&+\; \vartriangle_i\left(m\,\vec{Q}\right) \;+\; \vartriangle^+\left(m\,\vec{Q}\right) \\ &+\; \left(-P_c\,\vartriangle\vec{a} \;+\; \vartriangle_i p\,\vec{N} \;-\; \vartriangle^+\pi\,\vec{S}\right)\times\hat{k} \;=\; 0 \end{aligned} \tag{2.16}$$

It is advantageous to dot this into the $\vec{S}$ and $\vec{N}$ vectors. Using the vector relations

$$\vec{S}\cdot\left(\vec{S}\times\hat{k}\right) \;=\; 0 \qquad\qquad \vec{N}\cdot\left(\vec{N}\times\hat{k}\right) \;=\; 0$$

$$\vec{S}\cdot\left(\vec{N}\times\hat{k}\right) \;=\; -\vec{N}\cdot\left(\vec{S}\times\hat{k}\right) \;=\; \left(\vec{S}\times\vec{N}\right)\cdot\hat{k} \;=\; V$$

gives the S-momentum and N-momentum equation components

$$\begin{aligned} \frac{1}{V}\,\vec{S}\cdot\frac{\partial}{\partial t}\left((\rho\vec{Q})_a\, V\right) \;&+\; \vartriangle_i(m\,q\,f \;+\; m\,q_\perp f_\perp) \;+\; \vartriangle^+(m\,q\,f \;+\; m\,q_\perp f_\perp) \\ &+\; \vartriangle p \;-\; P_c\,\Theta_S \;=\; 0 \end{aligned} \tag{2.17}$$

$$\begin{aligned} \frac{1}{V}\,\vec{N}\cdot\frac{\partial}{\partial t}\left((\rho\vec{Q})_a\, V\right) \;&+\; \vartriangle_i(m\,q\,g \;+\; m\,q_\perp g_\perp) \;+\; \vartriangle^+(m\,q\,g \;+\; m\,q_\perp g_\perp) \\ &+\; \vartriangle\pi \;-\; P_c\,\Theta_N \;=\; 0 \end{aligned} \tag{2.18}$$

where the following convenient geometric factors have been used.

$$\begin{aligned} f_i \;&=\; \frac{\hat{s}_i\cdot\vec{S}}{V} \qquad f^+ \;=\; \frac{\hat{b}^+\cdot\vec{S}}{V} \qquad f_{\perp i} \;=\; \frac{\hat{s_{\perp i}}\cdot\vec{S}}{V} \qquad f^+_\perp \;=\; \frac{\hat{b^+_\perp}\cdot\vec{S}}{V} \\ g_i \;&=\; \frac{\hat{s}_i\cdot\vec{N}}{V} \qquad g^+ \;=\; \frac{\hat{b}^+\cdot\vec{N}}{V} \qquad g_{\perp i} \;=\; \frac{\hat{s_{\perp i}}\cdot\vec{N}}{V} \qquad g^+_\perp \;=\; \frac{\hat{b^+_\perp}\cdot\vec{N}}{V} \end{aligned}$$

$$\Theta_S \;=\; \frac{1}{V}\,(\vec{b}^+\times\vec{b}^-)\cdot\hat{k} \qquad\qquad \Theta_N \;=\; \frac{1}{V}\,(\vec{a}_i\times\vec{a}_{i-1})\cdot\hat{k}$$

The N-momentum equation (2.18) must be manipulated further to eliminate the interim pressure variable π, which is not independent in light of the consistency

constraint (2.13). An additional constraint on π is

$$\pi_j^- \;=\; \pi_{j-1}^+ \tag{2.19}$$

since these π values between two adjoining streamtubes j and $j-1$ are in fact the same quantity and must be equal at all times. Using this relation together with the combination

$$\Big[\text{Equation(2.18)}\Big]_j \;+\; \Big[\text{Equation(2.18)}\Big]_{j-1} \;+\; 2\Big[p_a + P_c - \pi_a\Big]_j \;-\; 2\Big[p_a + P_c - \pi_a\Big]_{j-1}$$

results in the *reduced N-momentum equation* which is now devoid of the π variables.

$$\begin{aligned}
&\left[\frac{1}{V}\,\vec{N}\cdot\frac{\partial}{\partial t}\Big((\rho\vec{Q})_a\,V\Big) \;+\; \Delta_i(m\,q\,g \;+\; m\,q_\perp g_\perp) \;+\; \Delta^+(m\,q\,g \;+\; m\,q_\perp g_\perp) \;-\; P_c\,\Theta_N\right]_j \\
+\;&\left[\frac{1}{V}\,\vec{N}\cdot\frac{\partial}{\partial t}\Big((\rho\vec{Q})_a\,V\Big) \;+\; \Delta_i(m\,q\,g \;+\; m\,q_\perp g_\perp) \;+\; \Delta^+(m\,q\,g \;+\; m\,q_\perp g_\perp) \;-\; P_c\,\Theta_N\right]_{j-1} \\
+\;&2\Big[\,p_a \;+\; P_c\,\Big]_j \\
-\;&2\Big[\,p_a \;+\; P_c\,\Big]_{j-1} \;\;=\; 0
\end{aligned} \tag{2.20}$$

This replaces the original N-momentum equation (2.18).

The discrete energy equation is

$$\frac{\partial}{\partial t}\Big((\rho E)_a\,V\Big) \;\;+\;\; \Delta_i\,(m\,H) \;+\; \Delta^+\,(m\,H) \;=\; 0 \tag{2.21}$$

The residual functions are now defined as

$$\mathcal{R}_m \;=\; \Delta_i m \;+\; \Delta^+ m \tag{2.22}$$

$$\begin{aligned}
\mathcal{R}_S \;&=\; \Delta_i(m\,\tilde{q}\,f \;+\; m\,q_\perp f_\perp) \;+\; \Delta^+(m\,q\,f \;+\; m\,q_\perp f_\perp) \\
&-\; \Delta p \;-\; P_c\,\Theta_S
\end{aligned} \tag{2.23}$$

$$\mathcal{R}_N \;=\; \Delta_i(m\,\tilde{q}\,g \;+\; m\,q_\perp g_\perp) \;+\; \Delta^+(m\,q\,g \;+\; m\,q_\perp g_\perp)$$

$$- \quad P_c\,\Theta_N \tag{2.24}$$

$$\mathcal{R}_p \;=\; 2\,p_a \;+\; 2\,P_c \tag{2.25}$$

$$\mathcal{R}_H \;=\; \triangle_i(m\,H) \;+\; \triangle^+(m\,H) \tag{2.26}$$

where $\tilde{q}$ is an upwinded speed described later. The overall equation set can now be tersely given as follows.

$$\frac{\partial}{\partial t}\left(\rho_a\,V\right) \;+\; \mathcal{R}_m \;=\; 0 \tag{2.27}$$

$$\frac{1}{V}\,\vec{S}\cdot\frac{\partial}{\partial t}\left((\rho\vec{Q})_a\,V\right) \;+\; \mathcal{R}_S \;=\; 0 \tag{2.28}$$

$$\left[\frac{1}{V}\,\vec{N}\cdot\frac{\partial}{\partial t}\left((\rho\vec{Q})_a\,V\right) \;+\; \mathcal{R}_N \;+\; \mathcal{R}_p\right]_j$$
$$+\quad\left[\frac{1}{V}\,\vec{N}\cdot\frac{\partial}{\partial t}\left((\rho\vec{Q})_a\,V\right) \;+\; \mathcal{R}_N \;-\; \mathcal{R}_p\right]_{j-1} \;=\; 0 \tag{2.29}$$

$$\frac{\partial}{\partial t}\left((\rho E)_a\,V\right) \;+\; \mathcal{R}_H \;=\; 0 \tag{2.30}$$

As a consequence of the definitions of q^b, ρ^b and H^b at the midpoint of $\vec{b}$, the steady-state operators of the mass (2.27), S-momentum (2.28), and energy (2.30) span three streamtubes. In contrast, the steady-state operator of the reduced N-momentum equation (2.29) spans four streamtubes. Figure 2-4 shows the stencils of the equations.

2.1.2 Boundary Conditions

The steady problem requires three boundary conditions at each conservation-cell inflow face, and one boundary condition at each x, y grid node all along the perimeter of the domain, as sketched in Figure 2-5. When studying a started supersonic inlet, the flow is subsonic downstream of the shock. One physical boundary condition is therefore required. When the flow remains supersonic all along its path, which is the case for a straight duct, imposing a physical boundary condition at the exit plane will result in an ill-posed problem. However, a condition is still required to ensure

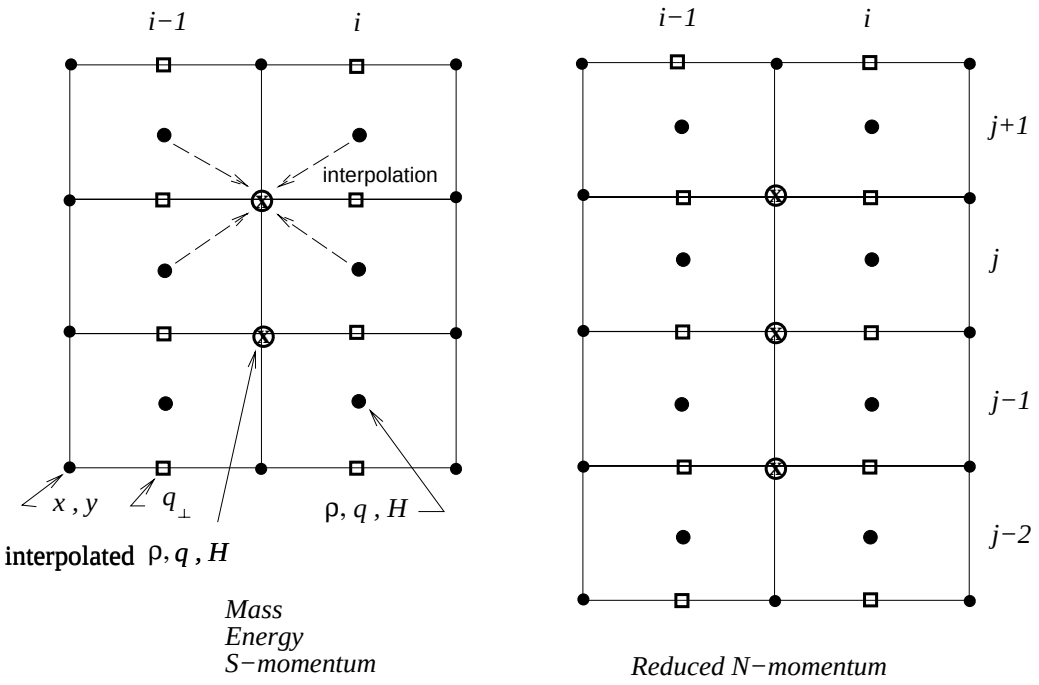

Figure 2-4: Stencils for the conservation equations and for interpolation at the midpoint of $\vec{b}$.

the uniqueness of the solution. A numerical boundary condition must therefore be imposed at the exit plane.

The total mass flow is not known a priori. This degree of freedom is constrained by specifying the *relative* mass flow between two adjacent streamtubes, but it is actually set by the outlet pressure. At each inflow face, the appropriate boundary conditions are as follows:

$$\left[m/\bar{m}\right]_j \;-\; \left[m/\bar{m}\right]_{j-1} \;=\; 0 \tag{2.31}$$

$$H \;-\; H_{\text{inlet}} \;=\; 0 \tag{2.32}$$

$$\mathcal{S} \;-\; \mathcal{S}_{\text{inlet}} \;=\; 0 \tag{2.33}$$

$$p \;-\; P_{\text{outlet}} \;=\; 0 \tag{2.34}$$

$$\text{where} \qquad \mathcal{S} \;\equiv\; h^{\gamma/(\gamma-1)}/p \quad , \quad h \;=\; H \;-\; \tfrac{1}{2}Q^2$$

The grid nodes at the inlet normally receive prescribed flow angles, and the nodes

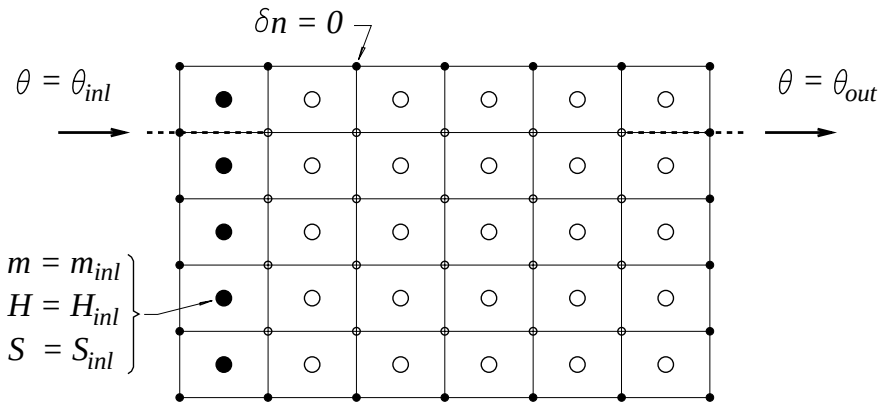

Figure 2-5: Steady boundary conditions for duct-flow problem. Variables associated with boundary condition residuals are indicated by solid circles. Variables associated with interior conservation equation residuals are shown as open circles.

on the bounding walls are allowed to slip along the wall:

$$\theta - \theta_{\text{inlet}} = 0 \tag{2.35}$$

$$\delta n_{\text{wall}} = 0 \tag{2.36}$$

$$\text{where} \qquad \theta = \arctan\left(Q_y/Q_x\right)$$

For the unsteady problem, the grid is no longer an unknown. The grid displacement is actually replaced by the normal component of the velocity $q_\perp$. Moreover, a better set of boundary conditions for the unsteady problem is to impose the incoming characteristic variables at the inlet. This replaces the total-enthalpy condition at the inlet [14]. The overall set of inlet and outlet boundary conditions is

$$\theta - \theta_{\text{inlet}} = 0 \tag{2.37}$$

$$J^+ - J^+_{\text{inlet}} = 0 \tag{2.38}$$

$$\mathcal{S} - \mathcal{S}_{\text{inlet}} = 0 \tag{2.39}$$

$$p - P_{\text{outlet}} = 0 \tag{2.40}$$

$$\text{where} \qquad J^+ \equiv \frac{Q}{2} + \frac{c}{\gamma - 1} \tag{2.41}$$

which is illustrated in Figure 2-6.

On each wall, we can impose the flow tangency condition in a straightforward way:

$$q_\perp \;=\; 0 \tag{2.42}$$

Air bleeding is one possibility of controlling shock motion. It consists in dumping a certain percentage of the inlet mass flow through different slots located on the walls. Since $q_\perp$ represents the normal-to-gridline component of the flow velocity, this formulation handles air bleeding quite easily, as follows:

$$q_\perp \pm \frac{\dot{m}}{\rho} \;=\; 0 \tag{2.43}$$

where $\dot{m}$ is the bleed mass flux per unit length. The '+' or '−' sign actually depends on the wall to be dumping air as can be seen in Figure 2-6.

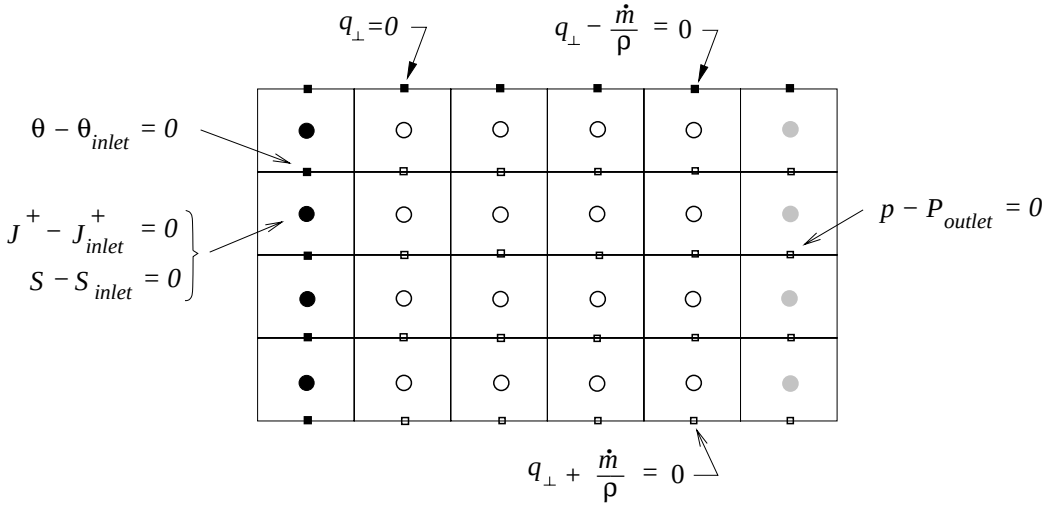

Figure 2-6: Unsteady boundary conditions for duct-flow problem.

J^- should also be imposed at the inlet plane when the inlet flow is supersonic. This is implicitly accounted for through the use of the upwinded speed $\tilde{q}$, which we will soon describe.

2.1.3 Artificial Dissipation

Dissipation is introduced via the upwinded speed $\tilde{q}$ which appears in the residual functions (2.23) and (2.24). It is defined as

$$\tilde{q}_i \;=\; q_i \;-\; \mu_i^{(1)}\,(q_i - q_{i-1}) \;+\; \mu_i^{(2)}\,(q_{i-1} - q_{i-2}) \tag{2.44}$$

where the numerical viscosity coefficients μ are defined in terms of the local Mach number.

$$\mu_i^{(1)} \;=\; \max\left[\,0\,,\; \frac{C_\mu}{\gamma}\left(1 \;-\; \frac{2\,M_{\rm crit}^2}{M_i + M_{i-1}}\right)\right] \tag{2.45}$$

$$\mu_i^{(2)} \;=\; \begin{cases} 0 \quad ; & \text{1st-order dissipation} \\ \mu_i^{(1)} \quad ; & \text{2nd-order dissipation} \end{cases} \tag{2.46}$$

$$C_\mu \;\simeq\; 1 \qquad\qquad M_{\rm crit} \;\simeq\; 0.98 \tag{2.47}$$

The dependence of $\tilde{q}_i$ on the $i-1$ and $i-2$ stations increases the upstream extent of the stencils of the $\mathcal{R}_S$ and $\mathcal{R}_N$ residual functions, as shown in Figure 2-7 for the S-momentum case.

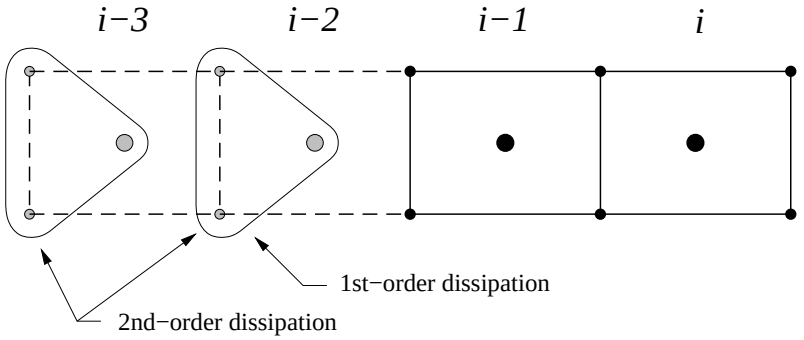

Figure 2-7: S-momentum stencil extension caused by introduction of 1st-order and 2nd-order dissipation.

$\tilde{q}$ implicitly sets J_{inlet}^- through the use of Q_{inlet} in the first two control cells. Indeed, setting J_{inlet}^+ and inlet velocity Q_{inlet} is equivalent to setting both Riemann's invariants.

2.1.4 Corrected Pressure Term

Since the $q_\perp$ averaging, both on $\vec{a}$ and $\vec{b}$, is transparent to the scheme, $q_\perp$ saw tooth modes are likely to show up wherever the grid slope is not smooth enough. Although these modes cannot be completely removed, they can be controlled through the use of a pressure correction. Although it is a numerical artifact, this corrected pressure term P_c is based on the mass conservation equation for a streamtube:

$$\dot{m} \;=\; \rho\, A\, Q \tag{2.48}$$

where A is the cross section area of the streamtube, and Q the speed of the flow. When $\dot{m}$ is held constant, we get:

$$\frac{dA}{A} \;=\; -\frac{dQ}{Q} \tag{2.49}$$

We can plug into

$$p \;=\; \frac{\gamma-1}{\gamma}\,\rho\left(H \;-\; \tfrac{1}{2}Q^2\right) \tag{2.50}$$

where ρ and H are held constant. We finally get:

$$dp \;=\; \frac{\gamma-1}{\gamma}\;\rho\; q^2\;\frac{dA}{A} \tag{2.51}$$

The corrected pressure term must be directly proportional to the streamtube area variation along the streamtube. However our grid is fixed and we cannot think of that approach in a geometric way. We actually write this streamtube area variation in terms of $q_\perp$. Although the grid is fixed, if $q_\perp$ fluctuates, the direction of the flow velocity fluctuates as well, and so does the streamtube area. This is better seen on Figure 2-8. This method is artificial, but it proved to be quite efficient in the original steady MSES, where the area variation was directly connected to the nodes motion. Then we define A_c in two different ways:

$$A_c \quad = \quad A_1 \;+\; \frac{q^+_{\perp i-1}}{q_a}\,\frac{\Delta x}{2} \;-\; \frac{q^-_{\perp i-1}}{q_a}\,\frac{\Delta x}{2} \;=\; A_1 \;+\; \frac{q^+_{\perp i-1} \;-\; q^-_{\perp i-1}}{q_a}\,\frac{\Delta x}{2}$$

$$A_c \;=\; A_2 \;+\; \frac{q^+_{\perp i}}{q_a}\,\frac{\Delta x}{2} \;-\; \frac{q^-_{\perp i}}{q_a}\,\frac{\Delta x}{2} \;=\; A_2 \;+\; \frac{q^+_{\perp i} - q^-_{\perp i}}{q_a}\,\frac{\Delta x}{2}$$

which implies

$$A_c \;=\; \frac{A_1 + A_2}{2} \;+\; \frac{(q^+_{\perp i-1} - q^-_{\perp i-1}) - (q^+_{\perp i} - q^-_{\perp i})}{q_a}\,\frac{\Delta x}{4} \tag{2.52}$$

Plugging (2.52) into (2.51), we finally get:

$$P_c \;=\; \frac{\gamma - 1}{\gamma}\,\rho_a\, q_a\, \frac{\Delta x}{2\,(A_1 + A_2)}\,(q^+_{\perp i-1} \;+\; q^-_{\perp i} \;-\; q^-_{\perp i-1} \;-\; q^+_{\perp i}) \tag{2.53}$$

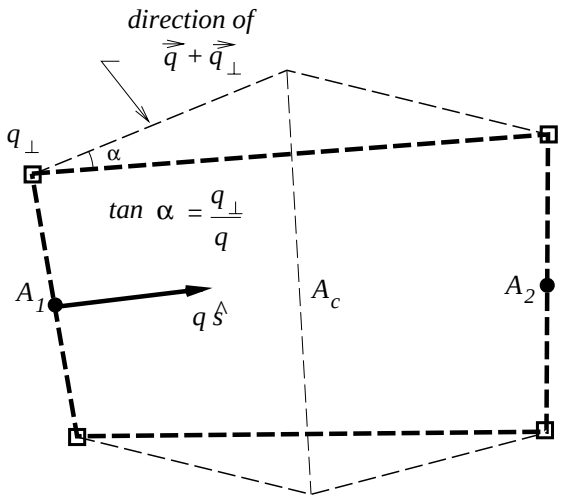

Figure 2-8: $q_\perp$ fluctuations and virtual streamtube area variations.

2.1.5 Nonlinear System

Variations in the inlet and exit conditions will be represented by the disturbance parameter vector **d**, whose length depends on the number of disturbances considered. Indeed, we could consider just a freestream density perturbation, which would affect several of the inlet quantities while the number of disturbances remains one.

The discrete nonlinear system of equations (2.27-2.30) can be written

$$\mathbf{F}\left(\dot{\mathbf{U}}\,,\,\mathbf{U}\,,\,\dot{\mathbf{m}}\,,\,\mathbf{d}\right)=0, \tag{2.54}$$

where $\mathbf{U}_i=[\rho^i,q^i,q^i_\perp,H^i]^T$ contains the state vector at every node, $\dot{\mathbf{m}}$ contains the bleed mass fluxes at each bleed location, and $\mathbf{d}$ contains the inlet and exit disturbances as described above.

Time discretization is done via a three point implicit scheme, therefore ensuring second order accuracy. At each time step, the resulting set of nonlinear equations is solved via Newton's method. The Jacobian is inverted with a LU solver. Storage and implementation of the formulation presented above is similar to the implementation described in [6].

All results presented in this dissertation are based on a fixed geometry. The actuation mechanism selected is mass flow bleeding. However, wall displacement could have been another possibility. Such a choice would have involve modifications of the grid geometry, which in turn would have become another perturbation input for system (2.54).

2.2 Linear formulation

Steady-state solutions can be evaluated by solving the nonlinear set of equations (2.54) where $\dot{\mathbf{U}}=0$. However, integrating the full nonlinear equation in time for unsteady flows is computationally expensive as it requires an LU factorization at each time step. If we limit ourselves to the consideration of small amplitude unsteady motions, the problem can be considerably simplified by linearizing the equations (2.27-2.30).

2.2.1 Linearized System

The unsteady flow and bleed input are assumed to be small perturbations about a steady state

$$\begin{aligned} \mathbf{U}(t) &= \overline{\mathbf{U}} + \mathbf{U}'(t) \\ \dot{\mathbf{m}}(t) &= \overline{\dot{\mathbf{m}}} + \dot{\mathbf{m}}'(t), \end{aligned}$$

and the unsteady inflow disturbances contained in $\mathbf{d}$ are assumed to be small. Performing a Taylor expansion about steady-state conditions and neglecting quadratic and higher order terms in $\dot{\mathbf{U}}'$ and $\mathbf{U}'$, the linearized form of equation (2.54) is

$$\frac{\partial \mathbf{F}}{\partial \dot{\mathbf{U}}} \frac{d\mathbf{U}'}{dt} + \frac{\partial \mathbf{F}}{\partial \mathbf{U}} \mathbf{U}' + \frac{\partial \mathbf{F}}{\partial \dot{\mathbf{m}}} \dot{\mathbf{m}}' + \frac{\partial \mathbf{F}}{\partial \mathbf{d}} \mathbf{d} = 0, \tag{2.55}$$

where all derivatives are evaluated at steady-state conditions. The above equation can be rewritten

$$E \frac{d\mathbf{U}'}{dt} + A\mathbf{U}' = B_m \dot{\mathbf{m}}' + B_d \mathbf{d}, \tag{2.56}$$

where the definitions of the matrices E, A, B_m and B_d follow directly from (2.55). Both E and A are $n \times n$ real matrices. It is important to note that while the boundary conditions may be set to time-varying quantities, they do not involve temporal differentiation. For example, a wall condition is of the form $q^{\perp}(t) = \dot{m}(t)/\rho$. Therefore, n_2 rows of E associated with the n_2 boundary condition equations are populated with zeroes exclusively: E is singular.

The parameter vector $\mathbf{d}$ essentially contributes to set the inlet and exit boundary conditions. Therefore, one may expect the non-zero entries of vector B_d to correspond only to boundary conditions. However, the first two S- and N- equations of each 'streamtube' also depend on parameter Q_i, inlet flow velocity, as a result of the upwinding scheme presented in section (2.1.3). Therefore non-zero entries are to be expected for these state equations.

2.2.2 Linearized Boundary Conditions

Here the perturbations caused by atmospheric disturbances and angle of attack changes are linearized. We only consider their first order effects. Therefore, to first order, a more general perturbation would be a linear combination of these effects. Note that all the following inlet flow quantities are implemented through inlet velocity Q_i, angle of attack θ_i, inlet speed of sound a_i and inlet entropy S_i.

Air bleeding

The linearization of the bleed condition (2.43) is straightforward:

$$q_\perp \pm \left(-\frac{\dot{m}_0}{\rho_0^2}\right).\rho \pm \frac{1}{\rho_0}.\dot{m} = 0 \tag{2.57}$$

where the subscript $_0$ refers to steady state quantities. To conform to the format used for equation (2.56), we can write it as:

$$q_\perp \pm \left(-\frac{\dot{m}_0}{\rho_0^2}\right).\rho = \mp \frac{1}{\rho_0}.\dot{m} \tag{2.58}$$

Isothermal vertical gust

Since the temperature is set to be constant, the inlet speed of sound remains unchanged. Among the four inlet quantities Q_i, θ_i, a_i and S_i, only Q_i varies, as follows.

$$\begin{aligned} Q_i &= Q_\infty + \triangle Q_i \\ \frac{v_i}{Q_i} \equiv \theta_i &= 0 \\ a_i &= a_\infty \\ \frac{h_i}{p_i^{(\gamma-1)/\gamma}} \equiv S_i &= S_\infty \end{aligned}$$

where v_i denotes the vertical component of the inlet velocity. In terms of the primary variables, this condition is:

$$
\begin{aligned}
\frac{Q_i}{2} + \frac{a_i}{\gamma - 1} \equiv J^+ &= J_\infty^+ + \frac{\Delta Q_i}{2} \\
\frac{Q_i}{2} - \frac{a_i}{\gamma - 1} \equiv J^- &= J_\infty^- + \frac{\Delta Q_i}{2} \\
\theta_i &= 0 \\
S_i &= S_\infty
\end{aligned}
$$

Atmospheric speed of sound (Temperature) change

Here we consider a constant pressure temperature change. Inlet velocity remains unchanged.

$$
\begin{aligned}
Q_i &= Q_\infty \\
\theta_i &= 0 \\
a_i &= a_\infty + \Delta a_i \\
S_i &= S_\infty + \frac{1}{p_\infty^{(\gamma-1)/\gamma}} \frac{2 a_\infty \Delta a_i}{\gamma - 1}
\end{aligned}
$$

Or, in terms of the primary variables:

$$
\begin{aligned}
J^+ &= J_\infty^+ + \frac{\Delta a_i}{\gamma - 1} \\
J^- &= J_\infty^- - \frac{\Delta a_i}{\gamma - 1} \\
\theta_i &= 0 \\
S_i &= S_\infty + \frac{1}{p_\infty^{(\gamma-1)/\gamma}} \frac{2 a_\infty \Delta a_i}{\gamma - 1}
\end{aligned}
$$

This perturbation is equivalent to a constant pressure density disturbance since $a = \sqrt{\gamma r T}$ only depends on the temperature T, as well as $\rho = p/(rT)$ when pressure is assumed to be constant.

To determine the unsteady response of the flowfield, the inputs $\dot{\mathbf{m}}'(t)$ and $\mathbf{d}(t)$ are specified as presented above and the large system (2.56) is time-marched to determine the resulting flow. Often, we are not interested in obtaining the actual flow itself, but in relevant output quantities. We define a output vector $\mathbf{y}$ as

$$\mathbf{y} = C\mathbf{U}' + D_m\dot{\mathbf{m}}' + D_d\mathbf{d} \tag{2.59}$$

which, for the analyses presented here, contains pressure sensing upstream of the shock and the average Mach number over the height of the inlet at a given location. C, D_m and D_d are matrices containing mean flow contributions to the output evaluation. To further simplify notation, we define the global input vector $\mathbf{u} = [\dot{\mathbf{m}}', \mathbf{d}]^T$ and rewrite equations (2.56) and (2.59) as

$$E\frac{d\mathbf{U}'}{dt} + A\mathbf{U}' = B\mathbf{u} \tag{2.60}$$

$$\mathbf{y} = C\mathbf{U}' + D\mathbf{u}. \tag{2.61}$$

In the subsequent discussion, we will only refer to perturbation about the steady state $\bar{\mathbf{U}}$. We may then drop the $'$ sign without ambiguity.

2.3 CFD Results

The main goal of the test cases presented in this section is to demonstrate the accuracy of the nonlinear formulation as well as the agreement between the nonlinear and the linear code for small perturbations.

2.3.1 Nonlinear Time Simulation

The nonlinear formulation is tested for a straight duct, whose length is five times its width. Although such a case does not demonstrate the full nonlinear capability of the formulation, we show that both convection and wave propagation are accurately simulated. Supersonic and subsonic regime are tested using two different inlet pertur-

bations, an incoming density disturbance and an incoming acoustic wave. These two disturbances are of interest since they do not propagate the same way. The incoming density wave is equivalent to an entropy wave. It is convected at the speed of the flow. The acoustic wave, a J^+ wave, propagates at the speed of sound relative to the mean flow.

Incoming Density Disturbance

The first test case is a duct flow with an inlet Mach number $M = 0.5$. An incoming density disturbance is generated which is constant across the inlet plane. It varies temporally with a Gaussian distribution as follows:

$$\rho'(t) = -0.01\rho_0 e^{-\alpha(t-t_{peak}/f_0)^2}. \tag{2.62}$$

where the frequency f_0 equals a_0/h, inlet speed of sound divided by the height of the inlet, and the non-dimensional time t_{peak} sets the time at which the perturbation peaks. In addition we set inlet velocity and pressure to their nominal value across the inlet plane. Such perturbation therefore convects at the speed of the flow. The time discretization scheme had a time step of length $1/2T_0$. For the results shown in Figure 2-9, $\alpha = 6f_0^2$ and $t_{peak} = 2$. Density was averaged across the width of the duct and plotted at streamwise stations for $t/T_0 = 2, 6, 10$ where $T_0 = 1/f_0$. The density distribution calculated by the code is plotted against the analytical solution for small perturbations:

$$\rho_2'(t) = -0.01\rho_0 e^{-\alpha(t-\frac{x}{c}-t_{peak}/f_0)^2}. \tag{2.63}$$

where $c = Q_i$ inlet velocity of the flow. No dissipation or dispersion is observed compared to the analytical solution.

The second test case has an inlet Mach number $M = 1.5$. A similar disturbance is generated with $\alpha = 12f_0^2$ and $t_{peak} = 1$. The time discretization scheme had a time step of length $1/4T_0$. Results are seen in Figure 2-10. Density was averaged across the width of the duct and plotted at streamwise stations for $t/T_0 = 1, 2.5, 4$. The density distribution is plotted against the analytical solution for small perturbations.

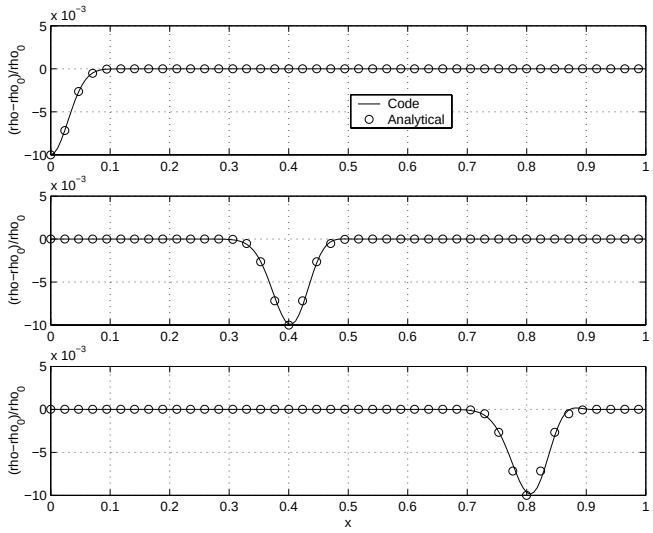

Figure 2-9: Subsonic flow $M = 0.5$ with 1% density disturbance at inlet. Density averaged over width plotted against analytical linear solution, as function of the x-coordinate. Top to bottom: $t/T_0 = 2, 6, 10$.

Very good agreement is observed.

Incoming Acoustic Wave

The next test case is a duct flow with an inlet Mach number $M = 0.5$. An incoming acoustic disturbance is generated which is constant across the inlet plane. This disturbance consists in a J^+ disturbance while J^- is held constant as well as entropy. It varies temporally with a Gaussian distribution as follows:

$$(J^+)'(t) = 0.005 J_0^+ e^{-\alpha(t - t_{peak}/f_0)^2}. \tag{2.64}$$

The speed of sound a can be easily obtained knowing that

$$\Delta a = (\gamma - 1)\, \Delta J^+ \tag{2.65}$$

The isentropic relationship

$$p/a^{\frac{2\gamma}{\gamma-1}} = constant \tag{2.66}$$

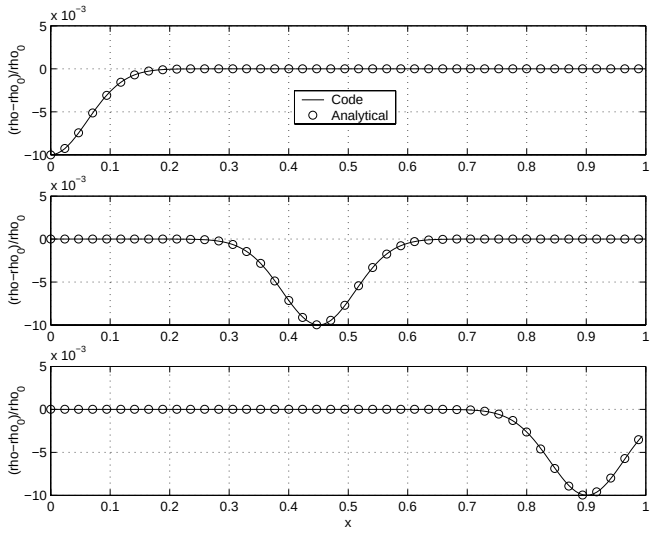

Figure 2-10: Supersonic flow $M = 1.5$ with 1% density disturbance at inlet. Density averaged over width plotted against analytical linear solution, as function of the x-coordinate. Top to bottom: $t/T_0 = 1, 2.5, 4$.

yields the inlet pressure, whose amplitude is 1.94 % of its nominal value. For the results shown in Figure 2-11, $\alpha = 12 f_0^2$ and $t_{peak} = 1$. The time discretization scheme had a time step of length $1/4T_0$. Pressure was averaged across the width of the duct and plotted at streamwise stations for $t/T_0 = 1, 2.5, 4.75$. The pressure distribution is plotted against the analytical solution for small perturbations with $c = a_0 + Q_i$. The propagation occurs without dissipation. The propagation speed c of the nonlinear flow response computed is slightly higher due to an increase in the local speed of sound.

The last case was computed for an inlet Mach number $M = 1.5$. A similar disturbance is generated with $\alpha = 20 f_0^2$ and $t_{peak} = 0.5$. The time discretization scheme had a time step of length $1/8T_0$. Results are seen in Figure 2-12. The amplitude of the incoming pressure perturbation is 1.11 % of its nominal value. Pressure was averaged across the width of the duct and plotted at streamwise station for $t/T_0 = 0.5, 1.25, 2$, against the analytical solution for small perturbations. As before, the match is quite satisfactory. As the simulation goes on, slight dissipation is observed. This effect is purely numerical and is due to the upwinding scheme which introduces a numerical

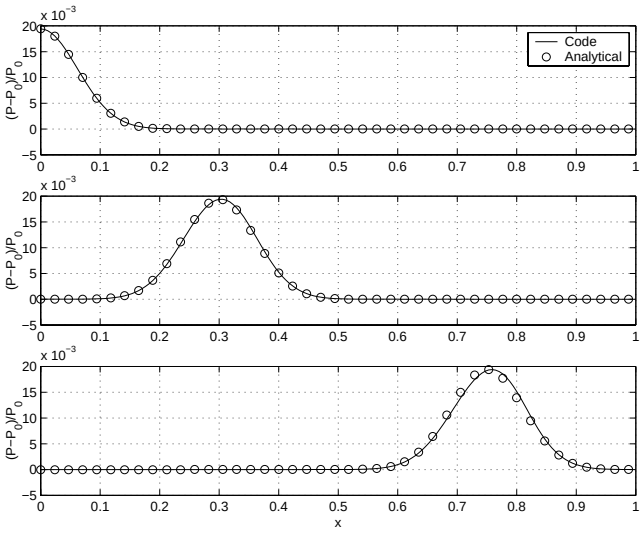

Figure 2-11: Subsonic flow $M = 0.5$ with incoming acoustic disturbance, 1.94% pressure perturbation. Pressure averaged over width plotted against analytical linear solution, as function of the x-coordinate. Top to bottom: $t/T_0 = 1, 2.5, 4.75$.

dissipation factor. Indeed, this acoustic wave creates a variation in the streamwise component of the flow, since $\Delta Q = \Delta J^+$. This effect may be reduced by decreasing the artificial dissipation factor, at the expense of potential numerical instabilities.

These computations have been done for small perturbations which does not completely demonstrate the nonlinear capability of the formulation. However, most of the applications presented later in this dissertation deal with linearized equations of the flow.

2.3.2 Linear Time Simulation

As this dissertation mostly focuses on the behavior of a diffuser at $M = 2.2$, both nonlinear and linear formulations are now compared for such supersonic flows. The steady state flow was computed for a freestream Mach number of 2.2. The inlet geometry and the Mach contours are shown in Figure 2-13. The diffuser is started as a shock forms right behind the throat. The Mach number averaged across the exit plane is 0.55.

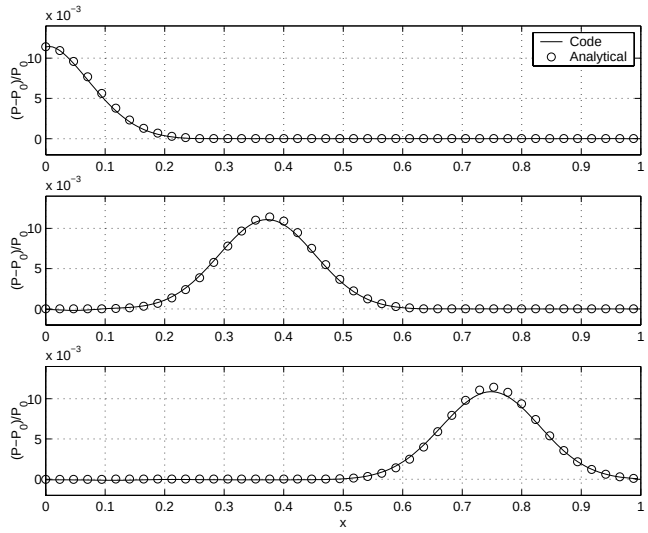

Figure 2-12: Subsonic flow $M = 1.5$ with incoming acoustic disturbance, 1.11% pressure perturbation. Pressure averaged over width plotted against analytical linear solution, as function of the x-coordinate. Top to bottom: $t/T_0 = 0.5, 1.25, 2$.

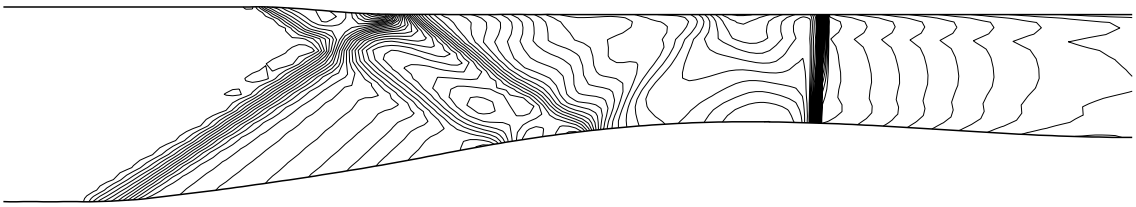

Figure 2-13: Mach contour of Mach 2.2 started flow in supersonic diffuser.

Good agreement is expected for small perturbations. Both nonlinear and linearized codes simulated the flow response in terms of Mach number averaged across the throat. An incoming density disturbance is set at the inlet plane, as described in the previous sub-section. Figure 2-14 shows the results for a 'fast' evolving Gaussian perturbation with parameters $\alpha = 2f_0^2$ and $t_{peak} = 5$. Three amplitudes were considered: 1 %, 2 % and 4 % of the nominal inlet density ρ_0. The time step was set to $1/T_0$. Nonlinear effects are weak and good agreement is observed for all three cases. Maximum error is defined as $max(M_l - M_{nl})/max(M_{nl} - M_0)$ where the subscripts $_l$, $_{nl}$ and $_0$ stand for the linear response, the nonlinear response and the nominal average

Mach number. The errors calculated are 2.5 %, 4.2 % and 7.8 % for amplitudes 1, 2 and 4 % respectively.

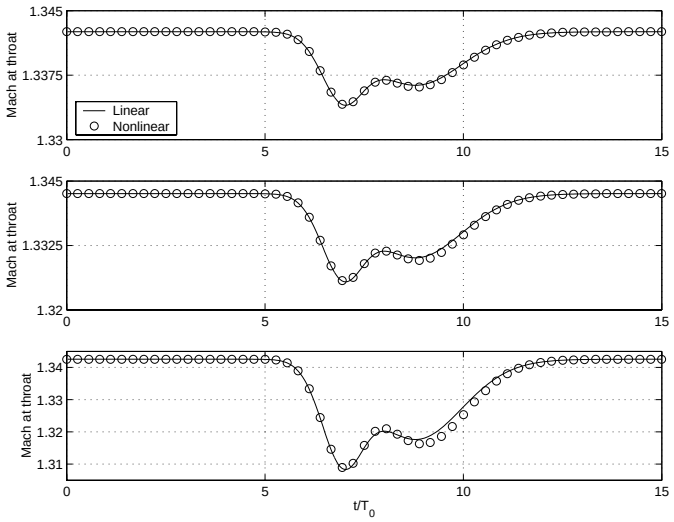

Figure 2-14: Inlet Mach number 2.2. Response to an incoming density disturbance $\alpha = 2f_0^2$ in terms of the average Mach number at the throat. Nonlinear response plotted against linearized response. Top to bottom: disturbance amplitudes are 1 %, 2 %, 4% of nominal density value.

As the temporal distribution of the disturbance is slowed down, accounting for nonlinear effects becomes crucial. Figure 2-15 shows the results of a similar time simulation with $\alpha = 0.03f_0^2$ and $t_{peak} = 20$. The time step was set to $1/0.3T_0$. Three amplitudes were considered: 1 %, 2 % and 3 % of the nominal inlet density ρ_0. While the error as defined above does not exceed 4 % for the 1 % density perturbation, it increases dramatically when reaching 2 % and becomes meaningless for 3 % due to the shock motion towards the throat. Although this last case remains stable, unstart is observed for disturbance amplitudes around 3.5 %.

Other computations showed that the shock motion amplitude is tied to the frequency content of the perturbation studied. This sets a lower bound to the maximum disturbance amplitude allowed to ensure good agreement between the nonlinear and linear formulations. Knowing the nature of the perturbations studied, this bound is actually set by the lowest frequency of interest. Nonlinear computations are therefore

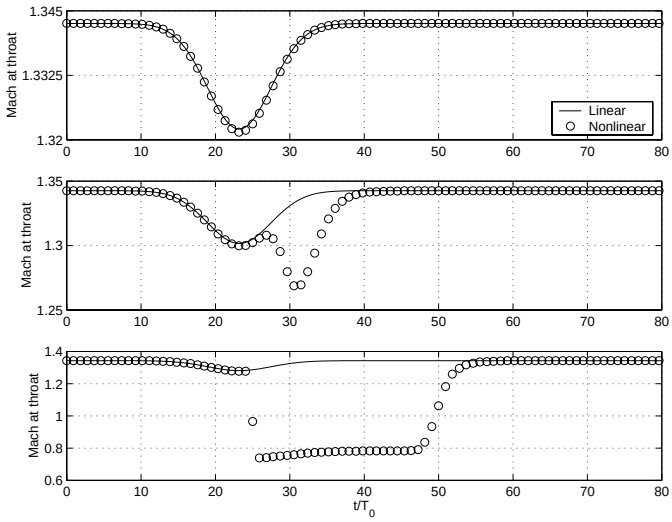

Figure 2-15: Inlet Mach number 2.2. Response to an incoming density disturbance $\alpha = 0.03 f_0^2$ in terms of the average Mach number at the throat. Nonlinear response plotted against linearized response. Top to bottom: disturbance amplitudes are 1 %, 2 %, 3% of nominal density value.

needed to estimate this threshold.

2.4 CFD Summary

A 2-D unsteady Euler flow solver designed for subsonic and supersonic flows in diffusers has been developed and validated against analytical solutions. A linearized formulation has been derived, which matches the nonlinear solver for small perturbations. However, the number of states of the CFD models is not well-suited for active control purposes. The next chapter will present methods to perform model-order reduction on the linearized solver.

Chapter 3

Arnoldi-based Model Order Reduction Techniques

In general, obtaining accurate results from a CFD code requires thousands of grid nodes so that the discretized equations correctly represent the continuous ones. Most of the results that are presented in this dissertation required more than 10,000 state variables when computed with a full-order CFD code (four unknowns at each grid point). Although we can restrict ourselves to linear perturbations around some pre-computed steady-state, the matrices involved are so large and so time consuming to solve that we cannot easily repeat simulations to get a good understanding of the system at hand. However, one is often concerned with a small set of outputs of interest due to a certain perturbation. The linear time invariant system to be reduced is given by the state space system (2.60,2.61). We drop the superscript $'$ to denote perturbations about the steady-state quantities.

The idea behind developing a projection-based reduced-order aerodynamic model is to project the large space used by a high-fidelity CFD model, such as that described in the previous chapter, onto a lower dimensional space which is characterized by a set of basis vectors. If these vectors are chosen so as to accurately span the solution space, the model behavior can be captured with just a few states. In this way a low-order, high-fidelity aerodynamic model can be obtained. There are several options available for selecting the basis vectors. We will focus on Arnoldi-based selection methods.

It is desirable to choose an orthogonal set of vectors, as the resulting congruent transformation preserves the system definiteness, and therefore often preserves system stability. The theory of Arnoldi-based model reduction will first be described for the generic system (2.60,2.61) and then extended for the case of singular descriptor matrix E.

If the set of q orthonormal basis vectors is contained in the columns of the matrix V, a qth order approximation to the perturbation solution can be made by assuming

$$\mathbf{U}(t) = V\hat{\mathbf{U}}(t), \tag{3.1}$$

where $\hat{\mathbf{U}}(t)$ is the reduced-order aerodynamic state vector. Substituting this representation of $\mathbf{U}$ into the linearized governing equations (2.60) we also require the residual $\mathbf{r}(t) = AV\hat{\mathbf{U}}(t) + B\mathbf{u} - EV\frac{d\hat{\mathbf{U}}}{dt}$ to be orthogonal to the subspace spanned by the columns of W i.e $W^T\mathbf{r} = 0$. This dissertation only makes use of $W = V$. As a result we obtain the reduced-order system

$$\hat{E}\frac{d\hat{\mathbf{U}}}{dt} + \hat{A}\hat{\mathbf{U}} = \hat{B}\mathbf{u}, \tag{3.2}$$

$$\hat{\mathbf{y}} = \hat{C}\hat{\mathbf{U}} + D\mathbf{u}, \tag{3.3}$$

where $\hat{E} = V^TEV$, $\hat{A} = V^TAV$, $\hat{B} = V^TB$, $\hat{C} = CV$ and $\hat{\mathbf{y}}$ is the output of the reduced-order system.

3.1 Arnoldi Basics

One approach to ensuring accurate representation of system dynamics is to try to match the transfer function of the reduced and original systems. Several different matching criteria are possible. Here we describe a process based on matching moments of the transfer function.

Consider the transfer function $H(s)$ of system (2.60) and (2.61):

$$H(s) \;=\; C\,(sE + A)^{-1}\,B \;+\; D, \tag{3.4}$$

which can be rewritten

$$H(s) \;=\; C\left(sA^{-1}E + I\right)^{-1}A^{-1}B \;+\; D \tag{3.5}$$

$H(s)$ can be expanded in a Taylor series about $s = 0$, resulting in the following expression:

$$H(s) \;=\; \sum_{k=0}^{\infty} m_k s^k \;+\; D \tag{3.6}$$

where

$$m_k \;=\; C\left(-A^{-1}E\right)^{k}A^{-1}B \tag{3.7}$$

is the kth moment of $H(s)$. A good approximation to the transfer function (3.6) about $s = 0$ should match its first moments m_k. One can think of the moments of the transfer function as being analogous to its derivatives evaluated at $s = 0$.

We now define the qth order Krylov subspace generated by a matrix A and a vector $\mathbf{b}$ as

$$\mathcal{K}_q\,(A\,,\,\mathbf{b}) \;=\; span\left\{\mathbf{b}\,,\,A\mathbf{b}\,,\,\ldots\,,\,A^{q-1}\mathbf{b}\right\} \tag{3.8}$$

The Arnoldi method generates a set of vectors which spans a qth order Krylov subspace, which is defined for the single-input, single-output system $E\dot{\mathbf{U}} = A\mathbf{U} + \mathbf{b}u$ as

$$\mathcal{K}_q\left(A^{-1}E\,,\,A^{-1}\mathbf{b}\right) \;=\; span\left\{A^{-1}\mathbf{b}\,,\,(A^{-1}E)A^{-1}\mathbf{b}\,,\,\ldots\,,\,(A^{-1}E)^{q-1}A^{-1}\mathbf{b}\right\} \tag{3.9}$$

Krylov subspace based projection techniques iteratively extract the dominant directions present in the time response to the chosen disturbance, like a power method extracts the dominant eigenvectors of a matrix. For a system with multiple inputs,

the Krylov subspace is generated by considering each input in turn:

$$\mathcal{K}_q\left(A^{-1}E, A^{-1}B\right) = \text{span}\{A^{-1}\mathbf{b}_1, (A^{-1}E)A^{-1}\mathbf{b}_1, \cdot, (A^{-1}E)^{q-1}A^{-1}\mathbf{b}_1, \\ A^{-1}\mathbf{b}_2, (A^{-1}E)A^{-1}\mathbf{b}_2, \cdot, (A^{-1}E)^{q-1}A^{-1}\mathbf{b}_2, \cdots\}, \qquad (3.10)$$

where $\mathbf{b}_1, \mathbf{b}_2, \cdots$ are the columns of B. As stated in [10], the essential elements of Krylov-subspace based reduction are given by

Lemma 1

Suppose $\mathcal{K}_q\left(A^{-1}E\,,\,A^{-1}B\right) \subset$ *colspan* (V), *then* $\left(A^{-1}E\right)^k A^{-1}B = V\left(\hat{A}^{-1}\hat{E}\right)^k \hat{A}^{-1}\hat{B}$, *for* $k < q$.

Proof: see Grimme [10].

This yields immediately the following moment matching theorem.

Theorem 1 (Krylov Subspace Model Reduction)

If colspan$(V) \subset \mathcal{K}_q\left(A^{-1}E\,,\,A^{-1}B\right)$ *then the reduced order transfer function* $\hat{H}(s) = \hat{C}\left(s\hat{E} + \hat{A}\right)^{-1}\hat{B} + D$ *matches the first* q *moments of the original transfer function* $H(s)$.

Proof: see Grimme [10].

Therefore, if V satisfies that condition in Theorem 1, the dynamics of our reduced-order model are expected to closely fit that of the full-order system as the disturbance frequency tends to $s = 0$. This theorem readily extends to non-zero frequencies as we shall see in next section.

3.2 Multiple Interpolation Point Arnoldi Method

The basic Arnoldi method results in a reduced-order model which matches coefficients of a Taylor series expansion of the full-order transfer function about $s = 0$. Although this means that low-frequency dynamics can be captured accurately with just a few reduced-order states, the model cannot be expected to be well-behaved as the disturbance frequency increases, or to accurately capture transient response. As the frequency range of interest increases, Arnoldi-based reduced-order models often require a large number of basis vectors to achieve accurate results. Instead of matching transfer function moments at zero frequency (the so-called time moments), an interesting extension is to shift the interpolation point to higher frequencies, or to consider multiple interpolation frequencies covering a wider frequency range.

Writing $s = s_0 + s'$, the Taylor series expansion of the transfer function (3.4) about some complex point s_0 yields

$$\begin{aligned} H(s) &= C\left(sE + A\right)^{-1} B + D \\ &= C\left[s'E + (A + s_0 E)\right]^{-1} B + D \\ &= C\left[s'\left(A + s_0 E\right)^{-1} E + I\right]^{-1} \left(A + s_0 E\right)^{-1} B + D \end{aligned}$$

We can therefore write

$$H(s) = \sum_{k=0}^{\infty} m'_k s'^k + D \tag{3.11}$$

where

$$m_k = C\left[-\left(A + s_0 E\right)^{-1} E\right]^k \left(A + s_0 E\right)^{-1} B \tag{3.12}$$

Equations (3.12) and (3.7) are equivalent, which can be seen by considering an analogous dynamical system in which $A \leftrightarrow (A + s_0 E)$ and $s \leftrightarrow s'$. The following statement is therefore a corollary of Theorem 1, as follows.

Corollary 1

If $colspan(V) \subset \mathcal{K}_q\left((A+s_0E)^{-1}E\,,\,(A+s_0E)^{-1}B\right)$ *then the reduced order transfer function* $\hat{H}(s) = \hat{C}\left(s\hat{E}+\hat{A}\right)^{-1}\hat{B}+D$ *matches the first* q *moments about* s_0 *of the original transfer function* $H(s)$.

Although Grimme [10] investigated both real and imaginary shifting in his very comprehensive work, we will focus on minimizing the frequency-response error $|\hat{H}(s)-H(s)|$ over a certain frequency range. Therefore, we will restrict this dissertation to imaginary interpolation points of the form $s_0 = i\omega_0$. We actually need to sample at s_0 and its complex conjugate s_0^*, for two reasons.

First, poles near the complex conjugate s_0^* might be 'forgotten' in the process when extracting dominant eigenvalues in the neighborhood of the imaginary interpolation point s_0. To motivate this observation, we note that the construction of the Krylov subspace involves the multiplication of vectors by $(A+s_0E)^{-1}E$. Let us expand some real vector $\mathbf{g}$ in terms of the generalized eigenvectors $\mathbf{x}_k$ of $(-A\,,\,E)$, with eigenvalues λ_k. After multiplying $\mathbf{g}$ by $(A+s_0E)^{-1}E$, whose eigenvalues are $1/(s_0-\lambda_k)$, we get (assuming distinct eigenvalues)

$$(A+s_0E)^{-1}E\mathbf{g} \;=\; (A+s_0E)^{-1}E\sum_{k=1}^{n}\alpha_k\mathbf{x}_k \;=\; \sum_{k=1}^{n}\frac{\alpha_k}{s_0-\lambda_k}\mathbf{x}_k \tag{3.13}$$

where α_k is the coordinate of $\mathbf{g}$ on the kth generalized eigenvector $\mathbf{x}_k$. Therefore eigenvalues that are strong (large α_k) or close to s_0 (large $1/\left(s_0-\lambda_k\right)$) are emphasized when multiplying $\mathbf{g}$ by $(A+s_0E)^{-1}E$. If the complex conjugate $(s_0^*-s_0)$ is large compared to the $(s_0-\lambda_k)$ that are emphasized, we might lose all the information contained by the poles close to s_0^*. At frequencies close to s_0, they are involved in the system dynamics though, and we might not get as good a local match as expected. However, this analysis is somewhat limited. See [10] for more details.

In addition to that, the use of complex matrices raises an important implementation concern: our reduced-order model should be consistent with the original system and yield real outputs. The avoidance of a complex basis V is therefore desirable. This is done by choosing s_0 and s_0^* pairwise: two Krylov subspaces $\mathcal{K}$ and $\mathcal{K}^*$ are

constructed, generated from sequences of vectors that are complex conjugate of each other, based on:

$$(A + s_0^* E)^{-1}\ \mathbf{g}^* \ = \ \left[(A + s_0 E)^{-1}\ \mathbf{g}\right]^* \tag{3.14}$$

No additional computational effort is involved in this method, since knowledge of the first sequence of vectors immediately implies knowledge of its conjugate. Moreover, the conjugate Krylov subspace $\mathcal{K}^*$ is not explicitly generated. The union space $\mathcal{K} \cup \mathcal{K}^*$ is the span of the real and imaginary parts of the vectors of $\mathcal{K}$. Only one set of vectors is computed, and V will be the set of the real and imaginary parts, after orthogonalization. This is best described in the pseudo-algorithm below for the single interpolation point $s_0 = i\omega_0$.

Algorithm 1 (Arnoldi method)

`function` V `= arnoldi(`E`,`A`,`$\mathbf{b}$`,`ω_0`,`q`)`

- `Factor` $(A + i\omega_0 E)$
- `Solve` $(A + i\omega_0 E)\,\mathbf{w} \ = \ \mathbf{b}$
- $\mathbf{V}_1 \ = \ \frac{\mathbf{w}}{\|\mathbf{w}\|}$
- `for` $j \ = \ 2 : q$
  - `Solve` $(A + i\omega_0 E)\,\mathbf{w} \ = \ E\mathbf{V}_{j-1}$
  - `for` $k \ = \ 1 : j-1$
    - $h \ = \ \mathbf{w}'\,\mathbf{V}_k$
    - $\mathbf{w} \ = \ \mathbf{w} - h\,\mathbf{V}_k$
  - `end`
  - $\mathbf{V}_j \ = \ \frac{\mathbf{w}}{\|\mathbf{w}\|}$
- `end`

Here, $\mathbf{w}'\,\mathbf{V}_k$ denotes the hermitian product of vectors $\mathbf{w}$ and $\mathbf{V}_k$. Each computed vector is orthogonalized with respect to the previous ones using a Gram-Schmidt orthogonalization process. Although this sub-step is not theoretically necessary, it enables numerical robustness as the number of vectors computed increases. If we

write $\mathbf{g} = \sum \alpha_k \mathbf{x}_k$, where $\mathbf{x}_k$ denotes the eigenvector of A with eigenvalue λ_k and k_0 the index of the dominant eigenvalue, $A^N \mathbf{g} \approx \lambda_{k_0}^N \alpha_{k_0} \mathbf{x}_{k_0}$ as N increases. Orthogonalization then plays a crucial role by preventing the resulting vector from being aligned with a dominant eigenvector.

The matrix V, as computed by Algorithm 3.1, which contains the q vectors $\mathbf{V}_j$ as columns, is an orthonormal basis for $\mathcal{K}_q$, with q complex basis vectors. V needs to be further processed to span $\mathcal{K}_q \cup \mathcal{K}_q^*$: the real and imaginary parts of each basis vector will be extracted, and the resulting $2q$ vectors orthogonalized. Gram-Schmidt appears to be a natural choice, and can be done at each step of Algorithm 1, in parallel with the Hermitian orthogonalization used for generation of the complex basis. However, an alternate approach is to perform the orthogonalization using singular value decomposition (SVD). Unlike Gram-Schmidt orthogonalization, SVD enables the assessment of the amount of new information added by each basis vector. Using the singular values, the option is available to further reduce the size of the resulting basis.

For the sake of simplicity, Algorithm 1 was restricted to a single interpolation point ω_0. This does not yield a better behaved model than the single point Arnoldi model derived about $s = 0$, as shown in Section 3.1: if a limited number of basis vectors are used, the reduced-order model will give a good match only in the neighborhood of ω_0. The range of accuracy of the model can be improved by using multiple interpolation points in order to obtain a good fit over the entire frequency range of interest. In the case of r interpolation points, the basis V spans $\cup_{q=1}^{r} \mathcal{K}_q$, which includes r Krylov subspaces by definition. Corollary 1 still holds, and moment matching is thus ensured at every interpolation point stored in $\omega = [\omega_0, \omega_1, \ldots, \omega_r]$. We can therefore evolve Algorithm 1 to consider r frequency points as follows. $\mathbf{q} = [q_1, q_2, \ldots, q_r]$ contains the numbers of complex Arnoldi vectors to be evaluated at each interpolation point ω_k.

Algorithm 2 (Multi-Point Arnoldi method)

`function` $\mathbf{V}$ `= arnoldi(`E`,`A`,`$\mathbf{b}$`,`ω`,`$\mathbf{q}$`,`r`)`

`for` $l = 1 : r$

```
    Q = ∑_{m=1}^{l-1} q_m
    Factor (A + iω_l E)
    Solve (A + iω_l E) w = b
    j = Q + 1
    V_j = w / ||w||
    for j = Q + 2 : Q + q_r
        Solve (A + iω_l E) w = E V_{j-1}
        for k = Q + 1 : j - 1
            h = w' V_k
            w = w - h V_k
        end
        V_j = w / ||w||
    end
end
```

As described previously, real and imaginary parts are then extracted and orthogonalization is done using SVD. At this time, the size of the basis can be further reduced. When the final set of basis vectors V is obtained, the reduced-order model is constructed by projection as described by equations (3.2) and (3.3). This method extends readily to multiple input cases by applying the algorithm to each column of B separately. The final basis is computed by recombining all the sets obtained from Algorithm 2 with SVD.

3.3 Application to Singular Descriptor Matrix Dynamical System

As seen in Section 2.2.1, the descriptor matrix E of system (2.60) is singular: we actually deal with an algebraic system. Although, the previous theorems apply to the singular descriptor matrix system [20], performing reduction via the Arnoldi method

directly on system (2.60) would not only reduce its dynamics but would also affect its boundary conditions. However, it is possible to extract an actual state-space system of order $n_1 = n - n_2$, whose dynamics are identical to (2.60). Boundary conditions will be put aside and treated separately. System (2.60) can be written

$$\begin{bmatrix} E_{11} & E_{12} \\ 0 & 0 \end{bmatrix} \begin{bmatrix} \dot{\mathbf{U}}_1 \\ \dot{\mathbf{U}}_2 \end{bmatrix} + \begin{bmatrix} A_{11} & A_{12} \\ A_{21} & A_{22} \end{bmatrix} \begin{bmatrix} \mathbf{U}_1 \\ \mathbf{U}_2 \end{bmatrix} = \begin{bmatrix} B_1 \\ B_2 \end{bmatrix} \mathbf{u}, \tag{3.15}$$

where $\mathbf{U}_2$ is a vector containing those flow unknowns which are prescribed via boundary conditions, and the vector $\mathbf{U}_1$ comprises the remaining unknowns, which are determined by the equations of state.

3.3.1 Condensed Dynamical System

Since the matrix A is invertible, the change of variables $\mathbf{U} = A^{-1}\mathbf{Z}$ can be applied. This change of variables does not alter the transfer function of the initial system and yields

$$\begin{bmatrix} \tilde{E}_{11} & \tilde{E}_{12} \\ 0 & 0 \end{bmatrix} \begin{bmatrix} \dot{\mathbf{Z}}_1 \\ \dot{\mathbf{Z}}_2 \end{bmatrix} + \begin{bmatrix} I_1 & 0 \\ 0 & I_2 \end{bmatrix} \begin{bmatrix} \mathbf{Z}_1 \\ \mathbf{Z}_2 \end{bmatrix} = \begin{bmatrix} B_1 \\ B_2 \end{bmatrix} \mathbf{u} \tag{3.16}$$

where $\tilde{E} = EA^{-1}$, and I_1 and I_2 are the identity matrices of dimensions n_1 and n_2 respectively. We also note that, for any matrix M, the structure of the matrix product EM remains identical to that of the matrix E: the transformed states $\mathbf{Z}_2 = A\mathbf{U}_2$ are prescribed.

The prescribed states $\mathbf{Z}_2$ can now be condensed out, leading to the actual state-space system

$$\tilde{E}_{11}\dot{\mathbf{Z}}_1 + \mathbf{Z}_1 = B_1\mathbf{u} - \tilde{E}_{12}B_2\dot{\mathbf{u}}, \tag{3.17}$$

where we have used $\mathbf{Z}_2 = B_2\mathbf{u}$. Denoting $\tilde{C} = CA^{-1} = \begin{bmatrix} \tilde{C}_1 & \tilde{C}_2 \end{bmatrix}$, the expression for the output $\mathbf{y}$ becomes

$$\mathbf{y} = \tilde{C}_1\mathbf{Z}_1 + \left(D + \tilde{C}_2 B_2\right)\mathbf{u}. \tag{3.18}$$

We will denote $\tilde{D} = \left(D + \tilde{C}_2\, B_2\right)$.

Using this change of variables, we have extracted the 'true' dynamics of system (2.60). Although the boundary conditions do not show up explicitly in equation (3.17), they can easily be reconstructed from $\mathbf{Z}_2 = B_2\mathbf{u}$. Moreover, they are implictly present in the output $\mathbf{y}$ due to the feedthrough term $\tilde{D}$.

3.3.2 Implementation of Arnoldi Method

The multiple frequency point Arnoldi reduction technique described is applied to the condensed state-space system (3.17, 3.18). The existence of a second input $\dot{\mathbf{u}}$ does not alter the method described previously, as shown by the transfer function

$$H(s) \;=\; \tilde{C}_1 \left(I_1 + s\tilde{E}_{11}\right)^{-1} \left(B_1 - s\tilde{E}_{12}B_2\right) \;+\; \tilde{D} \tag{3.19}$$

The presence of $\dot{\mathbf{u}}$ simply doubles the number of inputs to consider, since we can define a new set of moments generated by the term $\tilde{E}_{12}B_2$. Application of the multiple input, multiple frequency point Arnoldi method described above is unchanged, and the resulting basis spans the following Krylov subspace:

$$\mathcal{K}_q\Big\{ \left(I_1 + \omega_0\tilde{E}_{11}\right)^{-1} \tilde{E}_{11}, \left(I_1 + \omega_0\tilde{E}_{11}\right)^{-1} \left[B_1\,,\; \tilde{E}_{12}B_2\right] \Big\} \tag{3.20}$$

Due to the CFD formulation, boundary condition rows are mixed with state equations rows in $\tilde{E} = EA^{-1}$. It would not be practical to explicitly extract $\tilde{E}_{11}$ and $\tilde{E}_{12}$. Instead of computing V, an $n_1 \times q$ matrix, it is far more convenient to compute $\left[V^T \;\; 0\right]^T$ directly with the original system (3.16). The actual implementation is based on the following observations.

Inverse $\left(I + \omega_0\tilde{E}\right)^{-1}$

$$\left(I + \omega_0\tilde{E}\right)^{-1} \quad = \quad \begin{bmatrix} \left(I_1 + \omega_0\tilde{E}_{11}\right) & \omega_0\tilde{E}_{12} \\ 0 & I_2 \end{bmatrix}^{-1}$$

$$= \begin{bmatrix} \left(I_1 + \omega_0 \tilde{E}_{11}\right)^{-1} & -\omega_0 \left(I_1 + \omega_0 \tilde{E}_{11}\right)^{-1} \tilde{E}_{12} \\ 0 & I_2 \end{bmatrix} \tag{3.21}$$

Second input vector $\tilde{E}_{12} B_2$

$$\begin{bmatrix} \tilde{E}_{11} & \tilde{E}_{12} \\ 0 & 0 \end{bmatrix} \begin{bmatrix} 0 \\ B_2 \end{bmatrix} = \begin{bmatrix} \tilde{E}_{12} B_2 \\ 0 \end{bmatrix} \tag{3.22}$$

Multiplication by $\tilde{E}_{11}$

$$\begin{bmatrix} \tilde{E}_{11} & \tilde{E}_{12} \\ 0 & 0 \end{bmatrix} \begin{bmatrix} B_1 \\ 0 \end{bmatrix} = \begin{bmatrix} \tilde{E}_{11} B_1 \\ 0 \end{bmatrix} \tag{3.23}$$

Although we cannot extract the block matrix $\tilde{E}_{11}$, we can identify the entries corresponding to the matrix-vector product $\tilde{E}_{11} B_1$ in $\tilde{E}B$. These entries correspond to the n_1 actual state unknowns. Algorithm 2 is therefore applied to

$$\mathcal{K}_q \left\{ \left(I + \omega_0 \tilde{E}\right)^{-1} \tilde{E} \, , \, \left(I + \omega_0 \tilde{E}\right)^{-1} \begin{bmatrix} B_1 \\ 0 \end{bmatrix} \, , \, \left(I + \omega_0 \tilde{E}\right)^{-1} \tilde{E} \begin{bmatrix} 0 \\ B_2 \end{bmatrix} \right\} \tag{3.24}$$

The matrices $\tilde{E}$ or $\left(I + \omega_0 \tilde{E}\right)^{-1}$ are never explicitly computed. We actually make use of the following relations:

$$\tilde{E} \; = \; E \, A^{-1} \quad \text{and} \quad \left(I \; + \; \omega_0 \tilde{E}\right)^{-1} \; = \; A \, (A \; + \; \omega_0 E)^{-1}$$

Recombination of Krylov subspace vectors through SVD provides V. The final step consists in calculating the reduced model matrices as described by equations

(3.2) and (3.3).

$$\begin{aligned}
\hat{E} &= V^T \tilde{E}_{11} V = \begin{bmatrix} V^T & 0 \end{bmatrix} E A^{-1} \begin{bmatrix} V \\ 0 \end{bmatrix} \\
\hat{B}_1 &= V^T B_1 = \begin{bmatrix} V & 0 \end{bmatrix} \begin{bmatrix} B_1 \\ 0 \end{bmatrix} \\
\hat{B}_2 &= V^T \tilde{E}_{12} B_2 = \begin{bmatrix} V^T & 0 \end{bmatrix} E A^{-1} \begin{bmatrix} 0 \\ B_2 \end{bmatrix} \\
\hat{C} &= \tilde{C}_1 V = C A^{-1} \begin{bmatrix} V \\ 0 \end{bmatrix} \\
\tilde{D} &= D + \tilde{C}_2 B_2 = D + C A^{-1} \begin{bmatrix} 0 \\ B_2 \end{bmatrix}
\end{aligned}$$

3.4 Arnoldi-Based Model Order Reduction Summary

An algorithm has been presented to apply multiple point Arnoldi order reduction to large state space form systems. Multiple point Arnoldi method approximates the transfer function of the full-order model to be reduced over a frequency range defined by the user. The user picks frequencies in this range and computes Arnoldi vectors at each point. After recombining the Arnoldi vectors into an orthogonal real basis, the full-order model is projected onto this basis. The cost of computing the model lies in the number of frequency points, each of which implies one complex matrix inversion. The algorithm has also been generalized to singular descriptor matrix systems. The next chapter will present applications of this method on the linearized CFD model developed in Chapter 2.

Chapter 4

Results

Reduced-order models have been developed for supersonic started duct flows. A supersonic diffuser has been studied at a steady-state Mach number of 2.2 and a nominal upstream bleed of 1% of the inlet mass flow. The steady state Mach contours for this diffuser are shown in Figure 2-13. Figure 4-1 shows the different inputs and outputs of the system. The output of interest is the average Mach number at the throat in response to two unsteady inputs: a planar inlet density perturbation and an upstream bleed perturbation about nominal 1% bleed. Bleed occurs through small slots located between 46 % and 49 % of the inlet overall length. For control purposes, a sensor is located on the top wall, at the impingement point of the first Mach wave plotted on Figure 2-13. It measures pressure variations from the steady state pressure.

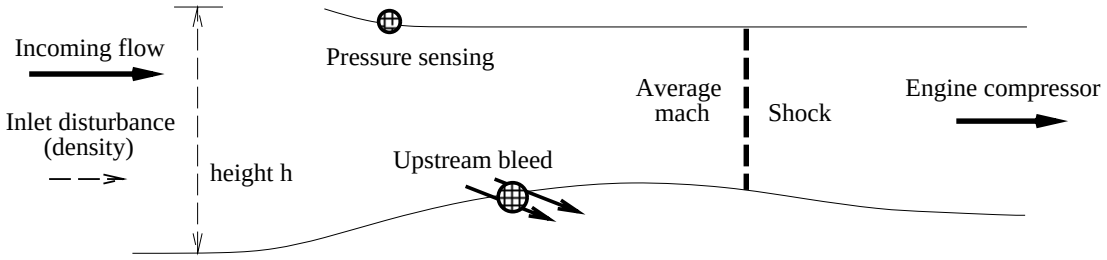

Figure 4-1: Definition of the different inputs and outputs: incoming density disturbance, air bleed, pressure sensing.

The CFD computational grid has 3078 points, which corresponds to 11,730 un-

knowns. A time-domain computation of this size is expensive, however we will show that the linearized flow dynamics can be accurately captured with less than 80 modes. All of the reduction methods shown are applied over the frequency range $[0, 2f_0]$ where $f_0 = a_0/h$ is the reference frequency of the diffuser, defined as the freestream speed of sound a_0 divided by the height h of the inlet. According to the atmospheric model considered, disturbances are expected to be in this range.

Throughout this chapter, we will refer to error between the full-order and the reduced-order transfer functions as the magnitude of $H(s) - \hat{H}(s)$, calculated at the complex frequency $s = 2\pi i f$. Maximum error will be the maximum value of this error over the frequency range $[0, 2f_0]$.

4.1 Unshifted Arnoldi Method

We begin with the basic Arnoldi method, which leads to a basis of vectors that matches moments of the transfer function about $s = 0$. Gram-Schmidt orthogonalization is performed sequentially from the first real vector computed to the last. Therefore, as we add one state to the model we increase the dimension of the spanned Krylov subspace by one and the reduced-order model obtained matches one more moment of the full-order transfer function. Figures 4-2 and 4-3 show the resulting gains and phases of the transfer functions from bleed input to average throat Mach number, for the full-order and reduced-order systems. In each plot, the dotted line corresponds to the full-order transfer function ($n = 11,730$). The solid lines are transfer functions for reduced-order models of size $q = 10, 20, 30, 40$ and 50, plotted from top to bottom. With just ten states in the reduced-order model, a good approximation is obtained locally near $f/f_0 = 0$, however for higher frequencies the error increases rapidly. As more Arnoldi vectors are added to the basis, the quality of the match improves for higher and higher frequencies. With 40 and 50 basis vectors, the transfer function is approximated well over the entire frequency range of interest. Although the size of the reduced-order models has increased to obtain this fit, we note that the computational expense to obtain each of the models shown in Figures 4-2 and 4-3 is of the

same order (i.e. the cost of a single system factorization).

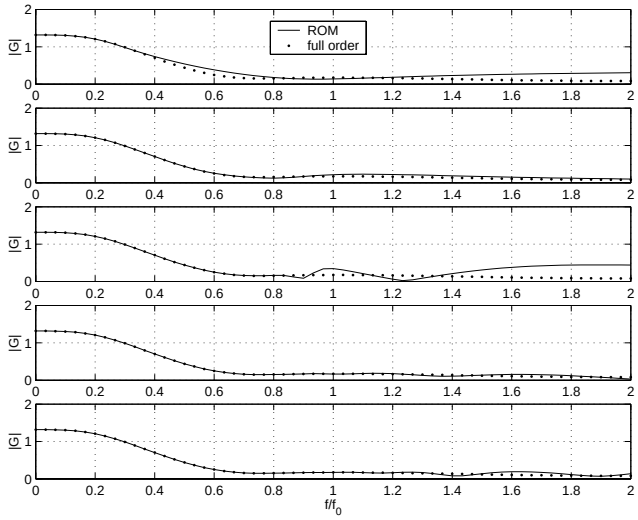

Figure 4-2: Magnitudes of full-order transfer function vs. ROM transfer function (bleed to average Mach number at throat). From top: 10, 20, 30, 40 and 50 reduced-order states, all models interpolated at $f/f_0 = 0$.

The evolution of accuracy with total number of modes is better shown in Figure 4-4. In this figure, the error at each frequency is plotted for the reduced-order models shown in Figures 4-2 and 4-3. It can be seen that with just 10 modes, the model is very accurate in the neighborhood of $f = 0$, and this local accuracy does not improve as more modes are added (due to round-off errors). Figure 4-4 shows clearly that as more modes are included in the model, the accuracy at frequencies away from the interpolation point increases. It is interesting to note that for the $q = 30$ case, the improvement in accuracy over the frequency range $[0, 0.8f_0]$ is achieved at the expense of a worse prediction at higher frequencies. This can also be clearly seen in Figures 4-2 and 4-3 and highlights the fact that these single point Arnoldi models can be unreliable far away from their interpolation point. In order for all errors over the frequency range to be less than 10^{-2}, more than 100 basis vectors were required in the reduced-order model.

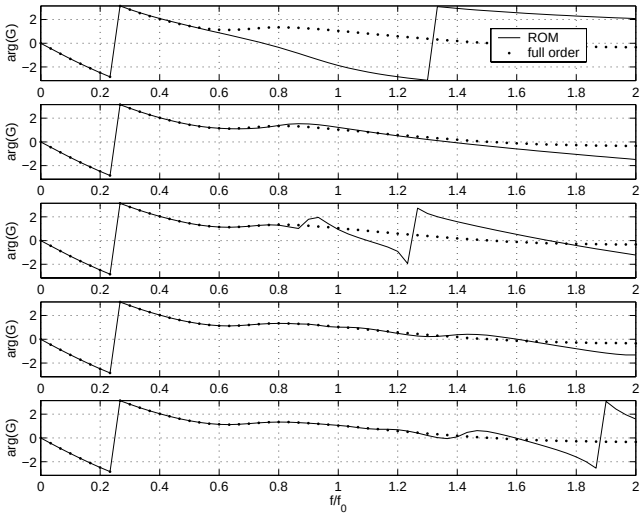

Figure 4-3: Phases of full-order transfer function vs. ROM transfer function (bleed to average Mach number at throat). From top: 10, 20, 30, 40 and 50 reduced-order states, all models interpolated at $f/f_0 = 0$.

4.2 Multiple-Point Arnoldi Method

While the previous results showed that the basic Arnoldi model required a large number of states to accurately capture the relevant dynamics over the frequency range, significant improvement can be realized by using the multiple-point Arnoldi method. As discussed, using multiple interpolation points causes moments of the transfer function to be matched at several frequencies. At each frequency chosen to be an interpolation point, the fit between the reduced-order and full-order transfer functions is *exact*. This can be seen in Figures 4-5 and 4-6 where results are shown using five frequency points: $f/f_0 = 0, 0.5, 1, 1.5$ and 2. The top plot in both Figures 4-5 and 4-6 is a reduced-order model of total size $q = 9$. This corresponds to one Arnoldi vector at each frequency point, calculated using Algorithm 2 and orthogonalized using Gram-Schmidt. Note, however, that the Arnoldi vectors at the non-zero frequency points are complex, and thus result in two basis vectors (total number of basis functions = 1+4*2 = 9). As the plot shows, the transfer functions of the reduced and full-order systems match exactly at the selected interpolation points.

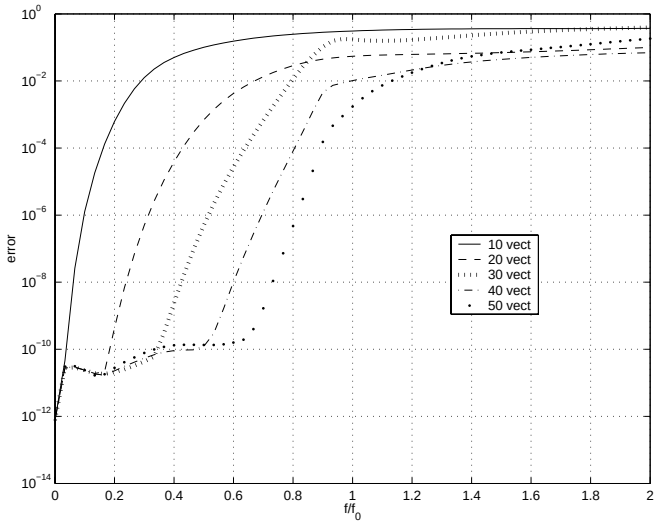

Figure 4-4: Absolute value of error for five reduced-order models of size 10, 20, 30, 40, 50. All models interpolated at $f/f_0 = 0$.

The size of the reduced-order model is increased by considering increments of one Arnoldi vector at each interpolation point. This results in reduced-order models of size $q = 18, 27, 36$ and 45, whose transfer functions are shown in the lower four plots of Figures 4-5 and 4-6 from top to bottom respectively. Figures 4-5 and 4-6 demonstrate the analogy between the moments and the derivatives of the transfer function. As discussed, in the top plot the value of transfer function at each interpolation point is matched exactly. In the second plot (two Arnoldi vectors and hence two moments matched per frequency point), it can be seen that the value of the transfer function plus its slope are matched. Figures 4-5 and 4-6 also show that as the number of Arnoldi vectors at each interpolation point is increased, the fit away from that frequency improves.

Figure 4-7 shows the error between the reduced-order and full-order transfer functions versus frequency for five models ranging in size from $q = 18$ to $q = 63$. For the four lower order models, the maximum error is of the order 10^{-1}. A significant reduction in error is achieved by including 63 state vectors. In this case, the maximum error over the frequency range of interest is 10^{-2}. For the single-point Arnoldi method, more than 100 basis vectors are required to achieve this level of accuracy.

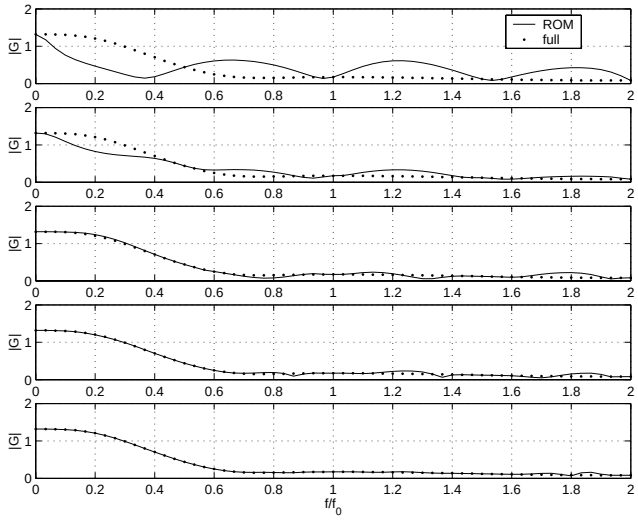

Figure 4-5: Magnitudes of full-order transfer function vs. ROM transfer function (bleed to average Mach number at throat). All models derived with five interpolation points at $f/f_0 = 0, 0.5, 1, 1.5, 2$. From top: 9, 18, 27, 36 and 45 reduced-order states.

Figure 4-7 shows clearly that for a low number of states, accuracy remains localized to the neighborhood of the interpolation points.

Gram-Schmidt was used to orthogonalize all the basis vectors for the multiple-point Arnoldi models described above. A better approach is to use SVD to perform this orthogonalization. Once the complex Arnoldi basis about each frequency point has been computed (which uses an internal Gram-Schmidt procedure), the set of real vectors resulting from the extraction of the real and imaginary parts can be combined and orthogonalized using SVD. This approach gives us the option to select a subset of the resulting orthogonal vectors, based on the calculated singular values. If not all of the vectors are retained, then the moment matching properties will not be preserved exactly. Figure 4-8 compares the results for both orthogonalization processes. A five point Arnoldi model was generated, identical to that discussed above. 90 real vectors were extracted from the initial complex vectors. Gram-Schmidt was used to perform orthogonalization and construct one set of reduced-order models, whose sizes range from 2 to 88 vectors. SVD was also performed on the 90 real vectors and another set of reduced-order models was constructed. Maximum error over $[0, 2f_0]$ is plotted for both

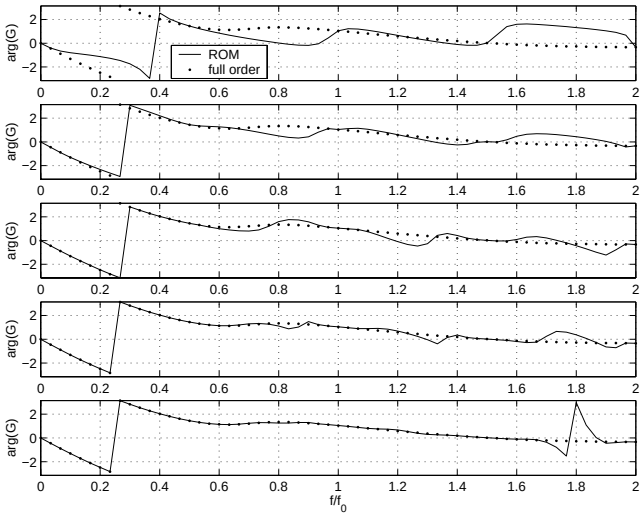

Figure 4-6: Phases of full-order transfer function vs. ROM transfer function (bleed to average Mach number at throat). All models derived with five interpolation points at $f/f_0 = 0, 0.5, 1, 1.5, 2$. From top: 9, 18, 27, 36 and 45 reduced-order states.

set of models from size 2 to 88 vectors. No significant difference can be seen before reaching low singular values. The gain in accuracy is then dramatic: SVD offers a maximum error of order 10^{-6} with 75 vectors while the error due to the Gram-Schmidt basis levels off at 10^{-4} and increases dramatically after that point. This shows that Gram-Schmidt orthogonalization is an ill-conditioned method compared to SVD. A slight increase in error is observed if an even higher number of vectors are retained. The singular values give a good indication of the importance of a particular mode, and neglecting those modes with small singular values was found to result in efficient reduced-order models without compromising accuracy.

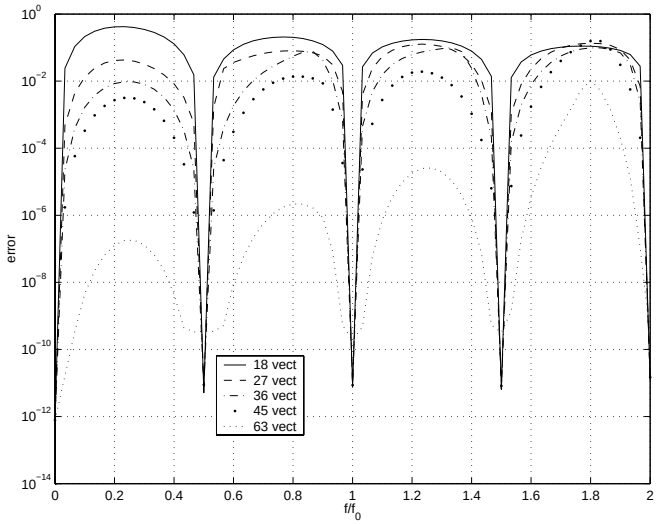

Figure 4-7: Absolute value of error for five reduced-order models of size 18, 27, 36, 45, 63. All models derived with five interpolation points at $f/f_0 = 0, 0.5, 1, 1.5, 2$.

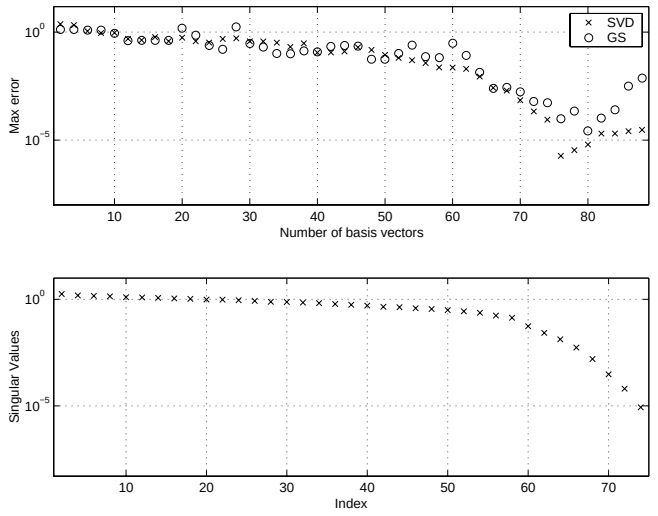

Figure 4-8: Comparison of Gram-Schmidt and SVD orthogonalization. Results are shown for 5 interpolation points at $f/f_0 = 0, 0.5, 1, 1.5, 2$. SVD basis was computed from a set of 90 vectors. Top: maximum error over $[0, 2f_0]$ versus number of basis vectors. Bottom: singular values.

4.3 From Multiple-Point Arnoldi to Proper Orthogonal Decomposition

Since the efficiency of the reduced-order model has been significantly increased by using the multiple-point Arnoldi method, the question might be asked: why not increase the number of interpolation points and reduce the number of moments matched per interpolation point? As discussed by Willcox et al. [27], as the number of frequency points is increased and the number of moments matched at each point is reduced to one, the method becomes a frequency-domain Proper Orthogonal Decomposition (POD) approach, which uses SVD on a set of complex responses obtained at selected frequency sample points to construct a basis [13, 15, 29].

A short aside may be useful to make the connection between the multiple point Arnoldi and the POD methods explicit. Fundamentally, the POD method aims at representing the solution $\mathbf{Z}(t)$ of the initial system (3.16) in an optimal way from a least-square perspective. We look for the vector $\mathbf{\Psi}(t)$ that satisfies

$$\max_{\mathbf{\Phi}} \frac{\langle |(\mathbf{Z}, \mathbf{\Phi})| \rangle}{(\mathbf{\Phi}, \mathbf{\Phi})} \;=\; \frac{\langle |(\mathbf{Z}, \mathbf{\Psi})| \rangle}{(\mathbf{\Psi}, \mathbf{\Psi})}. \tag{4.1}$$

where $(\ .\ ,\ .\ )$ and $\langle\ .\ \rangle$ denote scalar product and time averaging respectively. The vectors $\mathbf{\Psi}_k$ are the POD basis vectors computed as a linear combination of snapshots as follows:

- Choose a set of N frequency points ω_m in the frequency range of interest,
- Solve $\left(i\omega_m \tilde{E} + I\right) \mathbf{Z}_m \;=\; B$ for each frequency ω_m,
- Extract real and imaginary parts of each complex vector calculated: these are the in-phase and out-of-phase responses to the disturbance. The resulting N vectors form the snapshots $\mathbf{Z}_j$,
- Compute the correlation matrix C such that $C_{rp} = (\mathbf{Z}_r, \mathbf{Z}_p)\,/N$ and extract its eigenvalues as well as the associated eigenvectors $\mathbf{v}_k$,

- Construct each basis vector as a linear combination of snapshots using the eigenvectors as coefficients: the eigenvector $\mathbf{v}_k$ gives the basis vector $\mathbf{\Psi}_k = \sum_{j=1}^{N} \mathbf{v}_k^j \mathbf{Z}_j$.

This procedure is actually Algorithm 2 when computing only one complex Arnoldi vector at each frequency point. Moreover, it can be seen that calculating the correlation matrix C from the resulting real vectors and extracting its eigenvectors is equivalent to orthogonalizing them by SVD. The eigenvalues of C are in fact the singular values of the matrix whose columns are the real and imaginary parts of each complex vector computed. In this case, the POD basis is identical to an Arnoldi basis.

Figure 4-9 compares the accuracy provided by the multiple-point Arnoldi method and the POD method. The top plot shows the maximum error over the frequency range $[0, 2f_0]$. This error is plotted versus the total number of basis vectors in the reduced-order model for five approaches. The first three models use multiple-point Arnoldi with 5, 11 and 21 interpolation points. The baseline models in these three cases contained 90, 126 and 123 basis vectors respectively (corresponding to 11, 6 and 3 Arnoldi vectors respectively per frequency point). SVD was then used to select an orthogonal subset of the baseline vectors and create reduced-order models ranging in size from $q = 1$ to $q = 75$. The second two models shown in Figure 4-9 were created using POD with 41 and 61 frequency points, which yields baseline models of 81 and 121 vectors respectively. It can be seen that for models of size $q = 30$ or less, the maximum error is independent of the number of interpolation points. For higher-order models and lower error levels, the plot shows that, in most cases, choosing more frequency points improves the accuracy of the reduced-order model for a given number of basis functions. (When a very large number of basis vectors is selected, numerical noise becomes an issue, as can be seen for the 61-point POD method.) This improvement in accuracy must be traded with the computational cost of deriving the model, which is directly proportional to the number of interpolation points. The lower plot in Figure 4-9 shows the first 75 singular values for each of the models. While the POD singular values drop off more rapidly, the plot shows that there is considerable

advantage in post-processing the Arnoldi-based models with SVD to obtain a further reduction in size.

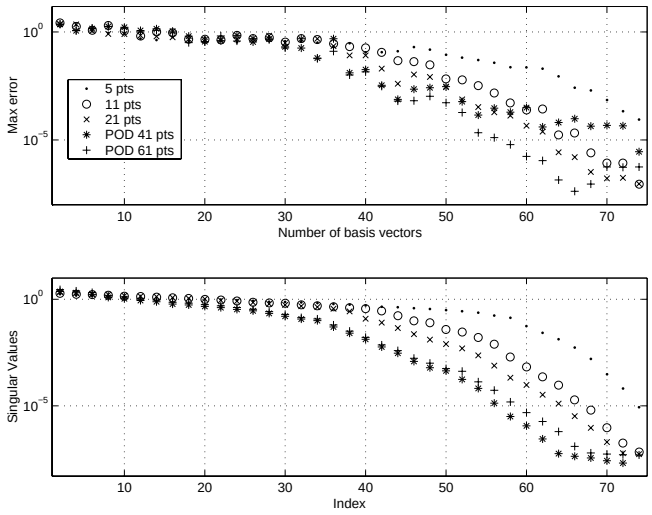

Figure 4-9: Comparison of multiple-point Arnoldi and POD models. Results are shown for Arnoldi models with 5, 11 and 21 interpolation points, and POD models with 41 and 61 interpolation points. Top: maximum absolute value of error over $[0, 2f_0]$ versus number of basis vectors. Bottom: singular values.

4.4 Multiple Input Arnoldi Method

As can be seen in Algorithm 2, the multiple-input Arnoldi method does not add complexity to the actual computation. For each input considered, a sequence of Arnoldi vectors is generated. A Gram-Schmidt procedure can be used to orthogonalize the resulting sequences of vectors. However, in order for moment matching properties to be satisfied exactly, all vectors must be retained in the basis. As the number of inputs increases, the size of the reduced-order model can become very large and also lead to numerical problems. Using SVD instead is a particularly convenient approach for the multiple input case. When the vectors are combined using SVD, there is no longer a separate sequence of vectors for each input. Instead, the resulting orthogonal basis can comprise a combination of Arnoldi vectors and have greatly

improved efficiency. As the singular values decrease, a subset of SVD vectors can be selected which offers similar accuracy properties.

Figure 4-10 shows the maximum error over the frequency range $[0, 2f_0]$ between a two input reduced-order and the full-order model. The two inputs considered are upstream bleed and incoming density disturbance. Two sets of Arnoldi vectors were generated separately using five frequency points: $f/f_0 = 0, 0.5, 1, 1.5$ and 2. Ten Arnoldi vectors were computed at each interpolation point yielding a 90 vector set for each input. They were recombined into a single orthogonal basis using SVD.

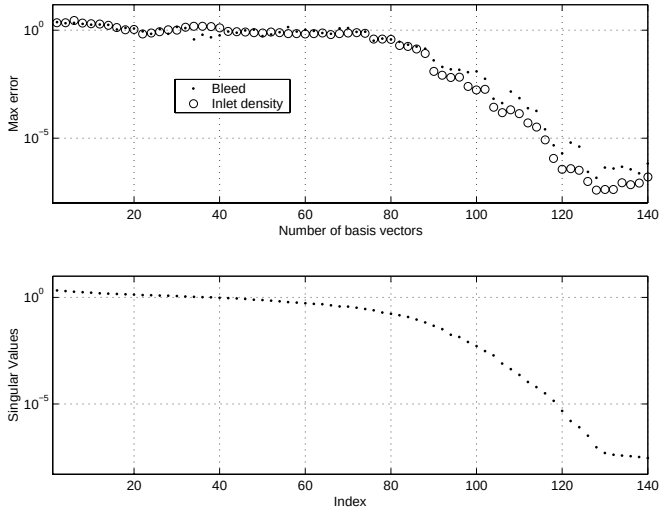

Figure 4-10: Two input reduced-order model Top: maximum absolute value of error over $[0, 2f_0]$ versus number of basis vectors. Bottom: singular values.

As seen in Figure 4-8, the single input five point Arnoldi model constructed for bleed required about 78 basis vectors to achieve an maximum error of order 10^{-5}. Although not shown, the trend is identical for the single input five point model constructed to simulate the effect of an incoming density disturbance. If we were to use Gram-Schmidt orthogonalization to recombine both sets of Arnoldi vectors, we would expect to need at least 155 basis vectors to reach this accuracy. However, after recombination with SVD, less than 120 state vectors are sufficient to reach this error level in Figure 4-10, demonstrating the efficiency of the recombination method. We also note the strong correlation between the singular values and the maximum error

observed. For more than two inputs, the SVD approach is expected to be even more efficient compared to Gram-Schmidt.

4.5 Time Domain Simulation

The following example demonstrates the accuracy of a multiple-point Arnoldi model for a time domain computation. For this case, we consider the second unsteady input to the system, an incoming density perturbation. Five interpolation points were used, at frequencies of $f/f_0 = 0, 0.5, 1, 1.5, 2$. Ten Arnoldi vectors were calculated at each interpolation point, resulting in a total of 90 vectors. These vectors were then combined and orthogonalized using SVD. The resulting singular values are plotted in Figure 4-11.

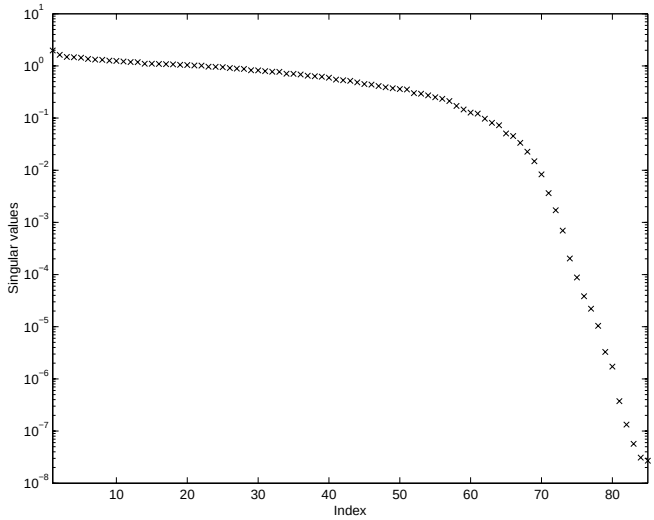

Figure 4-11: Singular values for the Arnoldi basis vectors for an incoming density perturbation.

The figure shows that the magnitude of the singular values starts to drop off rapidly once the basis reaches a size of approximately $q = 70$. Reduced-order models of varying size were constructed using the vectors obtained from the SVD analysis. Figure 4-13 shows a time-domain simulation of the diffuser in response to an incoming density perturbation calculated by the linearized CFD code and several reduced-order models. The perturbation considered is constant across the inlet plane, but varies

temporally with a Gaussian distribution as follows:

$$\rho'(t) = -0.02\rho_0 e^{-\alpha(t-2/f_0)^2}. \tag{4.2}$$

The parameter α in the above equation was selected so that the dominant frequency content of this perturbation falls in the range $[0, 2f_0]$. For the results shown in Figure 4-13, $\alpha = 6f_0^2$. Figure 4-12 shows the evolution of ρ' as a function of time.

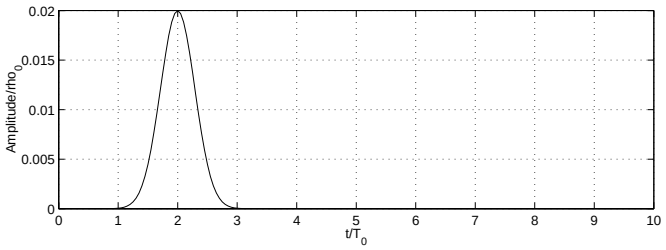

Figure 4-12: Incoming density disturbance as a function of time. $\alpha = 6f_0^2$, $T_0 = 1/f_0$.

The responses shown in Figure 4-13 support the conclusion drawn from the singular values in Figure 4-11. For models with $q = 40$ and $q = 50$, there is significant error in the time domain response. Increasing the number of modes to 60 gives a very good result, while the response with 70 modes is virtually indistinguishable from the CFD.

4.6 Active Control Design of Diffuser using Multiple-Point Arnoldi Method

Active control design is one of the fields that is the most sensitive to problem size. Even after linearization, CFD model are impracticable for control purposes. Reduced-order models that can capture the dynamics of the system in the frequency range of interest are therefore desirable. However, one must make sure that the models constructed accurately capture not only the dynamics of the initial system, but also the dynamics of the controlled system.

Throughout this section, we will develop a crude controller design to monitor the

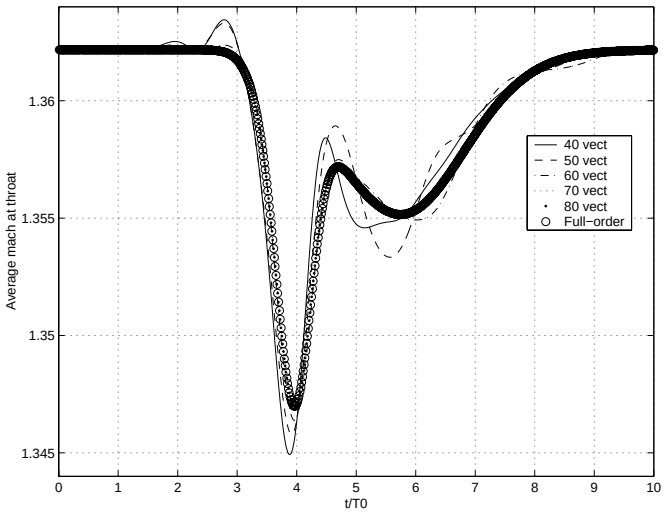

Figure 4-13: Linearized response to a density perturbation in the incoming flow. The full-order model (circles) is compared with several reduced-order models ranging in size from 40 to 80 states. $T_0 = 1/f_0$

average Mach variation over the throat of a supersonic engine inlet, in response to incoming flow variations. These results will not focus on the specifics of controller design, but rather are intended to demonstrate that a controller designed using reduced-order system dynamics is effective when applied to the full-order model.

4.6.1 Modeling and Control Design

Avoiding unstart is crucial for the flight safety of a supersonic jet. As the shock pops forward the aircraft structure undergoes a dramatic drag increase while the engine inlet mass flow drops far below the design value. We would like to control the shock position by limiting the amplitude of the throat Mach number variation. We make use of the same inputs and outputs described in Figure 4-1, which are as follows:

$$y = \frac{M_a - M_a^0}{M_a^0} \qquad \text{average Mach number variation}$$

$$z = \frac{p - p^0}{p^0} \qquad \text{pressure sensing}$$

$$d = \frac{\rho_{in} - \rho_{in}^0}{\rho_{in}^0} \qquad \text{incoming density disturbance}$$

$$b = \frac{\dot{m}_b}{\dot{m}_{in}} \qquad \text{fraction of mass flow dumped}$$

where M_a represents the Mach number averaged over the throat, p is the pressure

sensed, ρ_{in} the inlet density, $\dot{m}_b$ is the mass flow bled through the upstream slots, and $\dot{m}_{in}$ the incoming mass flow. These quantities are the full unsteady quantities (i.e $x = x^0 + x'$). The superscript ^{0} refers to the steady state.

Figure 4-14 supplements Figure 4-1 with the control path. The controller is a feedforward controller that evaluates the level of upstream bleed needed to limit the perturbation due to the incoming density disturbance, after assessing its importance via the upstream sensor.

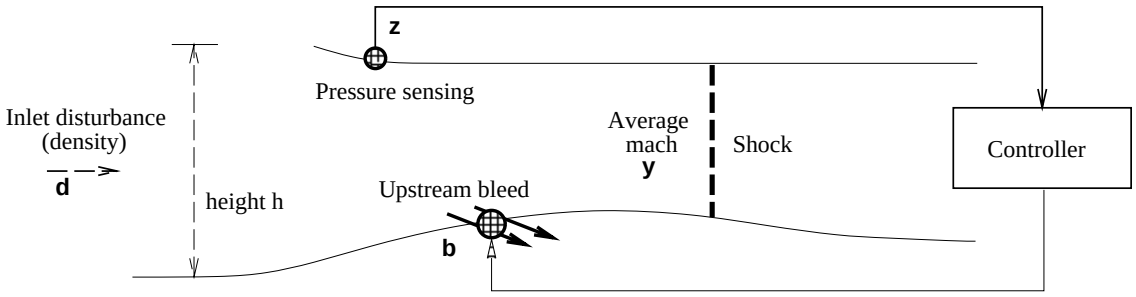

Figure 4-14: Control path for shock control: inlet disturbance, sensing, controller and actuation.

As discussed earlier, the atmospheric turbulence model used indicates that disturbances are expected to lie in the frequency range $[0, 2f_0]$. The controller design can therefore be restricted to this frequency domain.

The 2-D Euler equations are linearized as shown in section 2.2 and reduced with the multiple-point Arnoldi method. This requires identification of the inputs and outputs of the system. The main output y is the sum of the contributions y_d and y_a due to both disturbance d and actuation b respectively. The design considered focuses only on the supersonic flow upstream of the shock. As a result, the pressure sensed z, which is upstream of the actuation mechanism, is only affected by the incoming density disturbance and not by the actuation. We denote

$$y(t) = y_d(t) + y_a(t) \tag{4.3}$$

$$G(s) = \frac{Y_d(s)}{D(s)} \tag{4.4}$$

$$W_s(s) = \frac{Z(s)}{D(s)} \tag{4.5}$$

$$W_a(s) = \frac{Y_a(s)}{B(s)} \tag{4.6}$$

$$W_c(s) = \frac{B(s)}{Z(s)} \tag{4.7}$$

$$\tag{4.8}$$

where $X(s)$ denotes the Fourier Transform of $x(t)$. Figure 4-15 shows the block diagram connecting all the defined transfer functions.

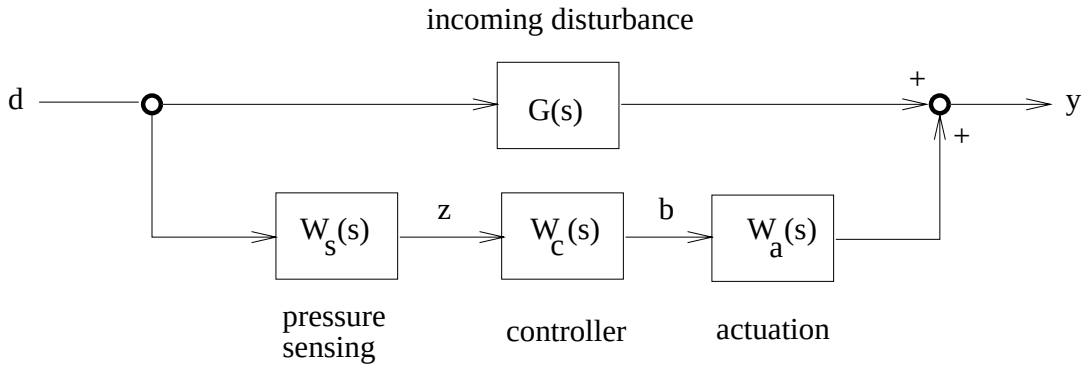

Figure 4-15: Block diagram of control system. Feedforward controller.

We can now explicitly write the relation between the controlled average Mach number variation y and the incoming density disturbance d in the Laplace space.

$$Y(s) = (G + W_a W_c W_s)\, D(s) \tag{4.9}$$

All three transfer functions G, W_a and W_s are known. However W_c must be determined. For this study, three reduced-order models were built to simulate the Mach response y_d to an incoming density disturbance d, the Mach response y_a due to bleed b, as well as the sensed pressure response z due to the inlet density perturbation d. For each model, five interpolation points were used, at frequencies of $f/f_0 = 0, 0.5, 1, 1.5, 2$. Ten Arnoldi vectors were calculated at each interpolation point, resulting in a total of 90 vectors. Only the input vector was accounted for

when generating the reduced basis V described in equation (3.1). (The Arnoldi basis does not consider output definition). As a result, the d-to-y and d-to-z models have the same low order matrices. The models are those shown in Figures 4-9 and 4-13. Referring to these results, we can limit the size of our reduced order model to 76 states. This allows very good accuracy to be achieved on the frequency range of interest. The transfer functions G, W_a and W_s based on the above reduced-order models were computed over the range $[0, 2f_0]$. They can be seen in Figure 4-16

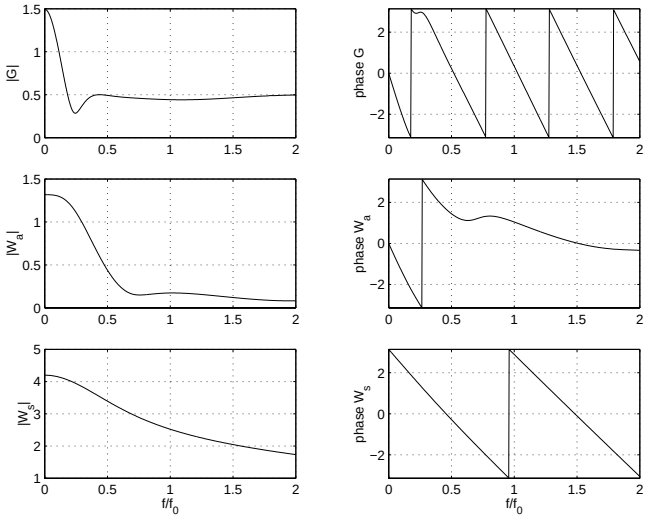

Figure 4-16: Gain (left) and phase (right) of the transfer functions of the system. From top to bottom: perturbation to be controlled G, actuation W_a and sensor W_s.

Once the reduced-order models have been generated, the input/output behavior can be evaluated at many frequencies with low computational cost. Each evaluation requires one system factorization and solve, which for the high-order system is expensive. For each of the transfer functions, five high-order system factorizations were required to derive the reduced-order models. The resulting models are then used to generate 100 data points over the frequency range of interest. To generate this amount of data with the original model would be computationally prohibitive.

The data generated by the reduced-order models were used to fit a lower-order model using the method of [18]. The controller transfer function W_c was then designed using H^∞ optimization [3]: adding a low pass filter to the input path,

$|(G + W_a W_c W_s)(i\omega)|$ was minimized over the range $[0, 1.5f_0]$ as the disturbance frequency most likely lies below f_0. The controller transfer function can be seen in Figure 4-17 and the closed-loop transfer function in Figure 4-18. Optimization was made more aggressive over the range $[0, 1.5f_0]$ at the expense of an ill-behaved response beyond $f = 1.5f_0$. Although the response amplitude increases dramatically for high frequencies, the controller remains stable. Significant improvement in Mach variation amplitude is obtained for frequencies below $0.6f_0$.

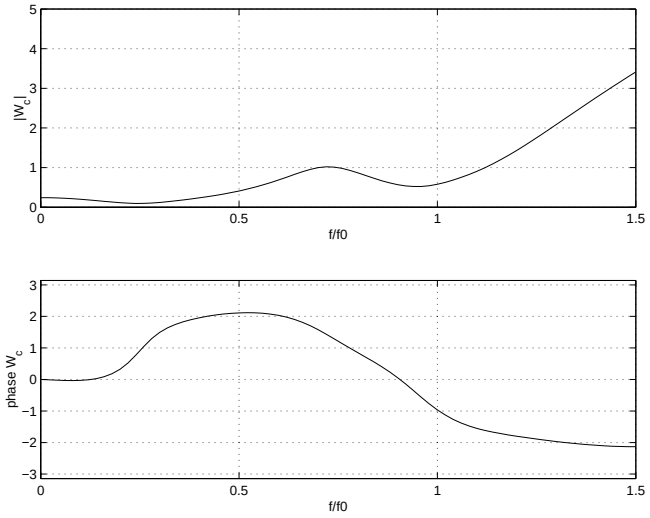

Figure 4-17: Gain and phase of the controller transfer function W_c.

4.6.2 Linearized CFD Model with Control versus Reduced-Order Model with Control

Although it was constructed using the reduced-order models, the interesting question is whether the controller will be effective for the high-order CFD model. The controller presented above was implemented in the full-order linear code and comparison was made of the Mach number response due to an incoming density disturbance of amplitude 1% of the nominal value ρ_0. Figure 4-19 shows the response y at the throat for both the linear code and the reduced-order model, when actuation is off and on. The inlet disturbance d has the form described in equation (4.2), with α set

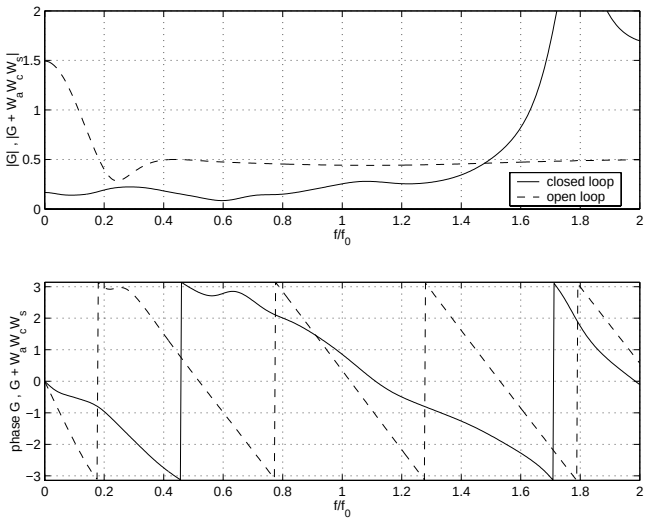

Figure 4-18: Gain and phase of closed-loop TF $(G + W_a W_c W_s)$ versus open-loop TF G. Optimization was stressed over $[0, 1.5f_0]$.

to $0.5f_0^2$ and peak time at $5T_0$. The frequency decomposition of this disturbance lies in $[0, 0.6f_0]$, which fits in the design frequency range of the controller.

Both the reduced-order and the full-order linearized model yield satisfactory response using the controller design presented previously. The reduced-order model response is virtually indistinguishable from that of the full-order linearized model. Under control, the CFD model has the behavior expected. This shows that the reduced-order models enable control design and accurate simulation of the CFD model response under control. Figure 4-20 represents the fraction of mass flow dumped though the bleed slots, for both models. Every parameter of interest is accurately represented with the reduced-order models used. Moreover, since the controller is effective at reducing the amplitude of the variation (as seen in Figure 4-19), the linearization assumption should hold for the controlled system. In future work, the effectiveness of the controller on the nonlinear system will be investigated.

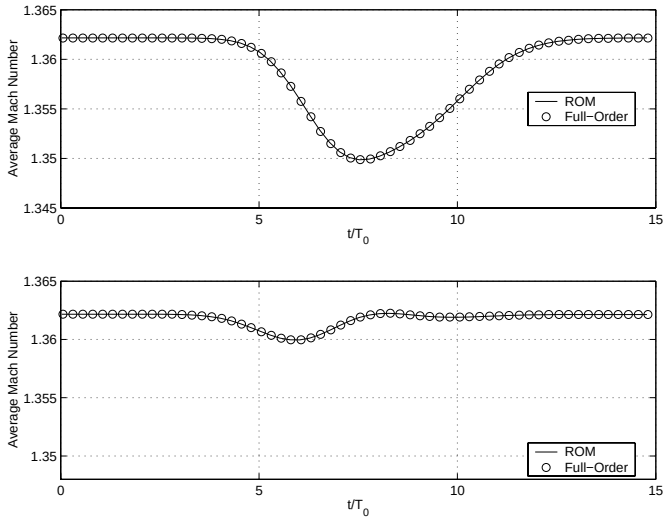

Figure 4-19: Mach number averaged over the throat as a function of time for full-order and reduced-order models. Top: control off. Bottom: control on. $T_0 = 1/f_0$.

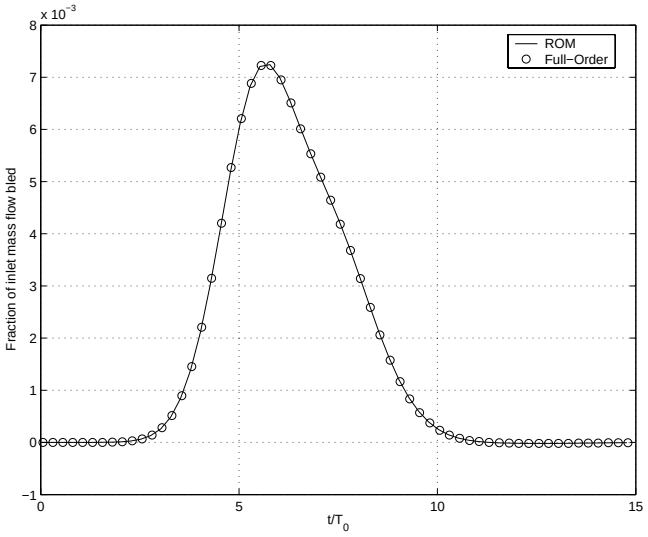

Figure 4-20: Fraction of inlet mass flow dumped through upstream slots, for full-order and reduced-order model.

Chapter 5

Conclusion and Recommendations

This dissertation presented a new computational tool for simulating unsteady Euler flow, and applied Arnoldi-based model-order reduction to the linearized equations derived from the flow solver. The resulting reduced-order models were used to design an active control strategy for a supersonic diffuser.

5.1 Unsteady Euler Flow Solver

This thesis first develops a method of discretizing the unsteady Euler equations for 2-D flows based on a finite-volume formulation. Flow velocity is represented locally using the grid geometry. It is decomposed into two components: its projection onto the meanline direction of the streamwise gridlines and its projection onto the direction normal to the streamwise gridlines. CFD validation results show that the formulation has subsonic and supersonic capability. Simple perturbations are simulated with high-fidelity. When simulating supersonic cases, a slight dispersion effect is observed due to the upwinding scheme added to ensure numerical stability. This effect can be reduced by tuning the artificial dissipation coefficient.

For model reduction purposes, this CFD formulation has been linearized. Good agreement is observed with the nonlinear formulation for small perturbations. Results show that, for supersonic started flows, nonlinear effects become more important as the frequency of the inlet disturbance is decreased. The linear system obtained from

the nonlinear solver is algebraic since the descriptor matrix is singular, as boundary conditions do not require temporal differentiation.

Even under the linearization assumptions, simulating such large fluid problems remains computationally expensive, or even impossible when considering optimal control design.

5.2 Arnoldi-Based Order Reduction Techniques

Reduced-order models are sought that accurately simulate flow responses due to selected disturbances, on a given frequency range. Basic and multiple interpolation point Arnoldi methods have been reviewed. Basis vectors are computed that span the Krylov subspace generated by iterating a complex matrix on the input vector. This input vector represents perturbations to the steady state boundary conditions. Real and imaginary parts of each complex basis vector are then extracted and recombined to form a single orthogonal basis. The full-order system is then projected onto this basis. Such methods allow matching of the first moments of the transfer function at each frequency point selected. This matching occurs only at zero frequency for the single point Arnoldi method. As the number of basis vectors increases, so does the number of moments matched at each point. This improves the frequency response of the reduced-order model. Two pseudo-algorithms have been presented to describe the sequence of the operations required by single and multiple point Arnoldi methods.

Since the linear system derived from the nonlinear formulation is algebraic, a specific implementation method has been developed for singular descriptor matrices. In this methodology, model order reduction is performed only on the state equations. Boundary conditions are extracted from the initial system and a state space system is derived from the state equations. The boundary conditions are not approximated and appear in the output via a direct transmission term.

Model order reduction techniques have been applied to the case of a supersonic diffuser whose flow is started. Results show the high-fidelity of the reduced-order models constructed for flows of interest. Model size was reduced by two orders of

magnitude from the original CFD model. When comparing full-order and reduced-order transfer functions, the use of multiple frequency points in the Arnoldi algorithm reduces the size of the required basis in order to achieve the same level of accuracy on the frequency range of interest. For example, using five frequency points results in a size reduction of 50 % over the single point model. Gram-Schmidt and singular value decomposition have been compared for recombination of the computed vectors. Not only does SVD yield faster convergence, but it also proves to be better numerically conditioned. This procedure also yielded additional accuracy information via the singular values. High-fidelity resolution is observed when comparing the transfer function of the full-order and the reduced-order models, as well as when performing time-simulation using both CFD and reduced-order models.

For the reduced-order models considered, the number of interpolation points and the number of Arnoldi vectors at each frequency point (and therefore the number of moments matched) were varied. These models were compared to POD-generated reduced-order models. When holding the number of state vectors constant, increasing the number of frequency points along with decreasing the number of Arnoldi vectors per frequency point improves accuracy for a given basis size. By balancing the number of frequency points and Arnoldi vectors per frequency point, the multiple point Arnoldi models can achieve roughly the same level of accuracy as POD models with the same number of basis vectors, but with a significant decrease in the cost of obtaining the model, as each frequency point requires one matrix inversion.

Two-input models have been constructed and compared against the original CFD model. CFD-quality frequency response has been observed for both inputs considered. SVD proves to be a convenient recombination method for the two sets of Arnoldi vectors generated, as it further reduces the number of state vectors required for achieving a given level of accuracy.

Arnoldi-based order reduction techniques have been applied to a simple control problem in the supersonic diffuser. Mach variations at the throat due to an incoming density disturbance are monitored via upstream bleed. Reduced-order models have been constructed to model disturbance, sensing and actuation. The limited size of the

models has allowed the evaluation of numerous data points which have been further processed to generate the controller design. When implementing the controller in both the full-order and the reduced-order model, discrepancies between time-simulations are indistinguishable, as long as the disturbance frequency lies in the design frequency range.

These results show that Arnoldi-based order reduction can model the flow response to any perturbation as accurately as the original CFD solver. Controlled dynamics of both full-order and reduced-order models are nearly indistinguishable. When performing model order reduction, the multiple point Arnoldi method is especially attractive as it offers a trade between accuracy and computational cost. The limited size of the model generated allows the application of optimal control theory. New perspectives are therefore offered to active flow control.

5.3 Recommendations for Future Work

There are several extensions that should be considered for this work:

- Simulate the presence of boundary layers on the walls via a wall blowing model. This would allow the code to account for viscous effects at low computational cost. Perform model order reduction on the pseudo-viscous code obtained.
- Validate the CFD model against experimental results.
- Identify the relevant quantities that can be related to the unstart mechanism.
- Investigate the actuator placement problem in order to optimize the effectiveness of the bleed device.
- Apply optimal control directly on the state space system generated via Arnoldi-based model-order reduction.
- Validate controller against experimental results.

- Investigate piecewise-linear model-order reduction to account for nonlinear effects such as shock motion.

Bibliography

[1] J.J. Adamczyk and M.E. Goldstein. Unsteady Flow in a Supersonic Cascade with Subsonic Leading-Edge Locus. *AIAA Journal*, 16(12):1248–1254, September 1978.

[2] Brian G. Allan. A reduced order model of the linearized incompressible navier-stokes equations for the sensor/actuator placement problem. *ICASE Report*, No. 2000-19, 2000.

[3] T. Basar and P. Bernhard. *H-infinity Optimal Control and Related Minimax Design Problems*, volume 2. Birkhauser, second edition, 1995.

[4] G. Berkooz, P. Holmes, and J.L. Lumley. The Proper Orthogonal Decomposition in the Analysis of Turbulent Flows. *Annual Review of Fluid Mechanics*, 25:539–575, 1993.

[5] E.H. Dowell, K.C. Hall, J.P. Thomas, R. Florea, B.I. Epureanu, and J. Heeg. Reduced Order Models in Unsteady Aerodynamics. AIAA Paper 99-1261, 1999.

[6] Mark Drela. *Two-Dimensional Transonic Aerodynamic Design and Analysis using the Euler Equations.* PhD thesis, Massachusetts Institute of Technology, 1985.

[7] J. Ffowcs Williams and X. Huang. Active stabilization of compressor surge. *Journal of Fluids Dynamics*, Vol. 204, 1989, pp. 245-262.

[8] W.R. Graham, J. Peraire, and K.Y. Tang. Optimal control of vortex shedding using low-order models. Part I - Open-loop model development. *International Journal for Numerical Methods in Engineering*, 44(7):945–972, 1999.

[9] W.R. Graham, J. Peraire, and K.Y. Tang. Optimal Control of Vortex Shedding Using Low-Order Models, Part II - Model-Based Control. *International Journal for Numerical Methods in Engineering*, 44(7):973–990, 1999.

[10] Eric James Grimme. *Krylov Projection Methods for Model Reduction.* PhD thesis, University of Illinois at Urbana-Champaign, 1997.

[11] K. C. Hall, J. P. Thomas, and E. H. Dowell. Proper orthogonal decomposition technique for transonic unsteady aerodynamic flows. *AIAA Journal*, 38(10):1853–62, October 2000.

[12] K.C. Hall. *A Linearized Euler Analysis of Unsteady Flows in Turbomachinery.* PhD thesis, Dept. of Aeronautics and Astronautics, MIT, May 1987.

[13] K.C. Hall. Eigenanalysis of Unsteady Flows About Airfoils, Cascades and Wings. *AIAA Journal*, 32(12):2426–2432, December 1994.

[14] C. Hirsch. *Numerical Computation of Internal and External Flows*, volume 2. Wiley, 1998.

[15] T. Kim. Frequency-Domain Karhunen-Loeve Method and Its Application to Linear Dynamic Systems. *AIAA Journal*, 36(11):2117–2123, 1998.

[16] D.J. Lucia, P.S. Beran, and P.I. Fing. Reduced-order modeling of an elastic panel in transonic flows. AIAA paper 2002-1594, 2002.

[17] David W. Mayer and Gerald C. Paynter. Prediction of supersonic inlet unstart caused by freestream disturbances. 1994.

[18] A. Megretski. Personal communication. April 2002.

[19] J.D. Paduano, A.H. Epstein, L. Valavani, J.P. Longley, E.M. Greitzer, and G.R. Guenette. Active Control of Rotating Stall in a Low-Speed Axial Compressor. *Journal of Turbomachinery*, 115:48–56, 1993.

[20] Joel R. Phillips. Automated extraction of nonlinear circuits macromodels. Proceedings of IEEE 2000 Custom Integrated Circuits Conference.

[21] M. Rewienski and J. White. A Trajectory Piecewise-Linear Approach to Model Order Reduction and Fast Simulation of Nonlinear Circuits and Micromachined Devices. Proceedings of the International Conference on Computer-Aided Design, San Jose, CA, Nov. 4-8, 2001.

[22] M.C. Romanowski. Reduced Order Unsteady Aerodynamic and Aeroelastic Models using Karhunen-Loéve Eigenmodes. AIAA Paper 96-194, 1996.

[23] L.M. Silveira, M. Kamon, I. Elfadel, and J. White. A Coordinate-Transformed Arnoldi Algorithm for Generating Guaranteed Stable Reduced-Order Models of RLC Circuits. *Computer Methods in Applied Mechanics and Engineering*, 169(3-4):377–389, February 1999.

[24] L. Sirovich. Turbulence and the Dynamics of Coherent Structures. Part 1 : Coherent Structures. *Quarterly of Applied Mathematics*, 45(3):561–571, October 1987.

[25] J.M. Verdon. Review of Unsteady Aerodynamic Methods for Turbomachinery Aeroelastic and Aeroacoustic Applications. *AIAA Journal*, 31(2):235–250, February 1993.

[26] D.S. Whitehead. Classical Two-Dimensional Methods. AGARD Manual on Aeroelasticity in Axial-Flow Turbomachines, Unsteady Turbomachinery Aerodynamics, Volume 1, 1987.

[27] K. Willcox, J. Peraire, and J. White. An arnoldi approach for generation of reduced-order models for turbomachinery. *Computers and Fluids*, 31:369.

[28] Karen E. Willcox. *Reduced-Order Aerodynamic Models For Aeroelastic Control of Turbomachinery*. PhD thesis, Massachusetts Institute of Technology, 2000.

[29] K.E. Willcox, J.D. Paduano, J. Peraire, and K.C. Hall. Low order aerodynamic models for aeroelastic control of turbomachines. *40th AIAA/ASME/ASCE/AHS/ASC Structures, Structural Dynamics and Materials (SDM) Conference*, 1999.